



**Politecnico
di Torino**

Master Thesis

Master of science in Electronic Engineering/Electronic Engineering Devices and
Technologies for Integrated Electronics and Optoelectronics

Multiphysics optimization of waveguide photodetectors for Silicon Photonics integrated circuits

Candidate:

Amin Shafiee

Supervisors

Prof. Michele GOANO, Advisor

Prof. Giovanni GHIONE, Co-Advisor

Dr. Alberto TIBALDI, Co-Advisor

Dr. Marco VALLONE, Co-Advisor

Politecnico di Torino

April 2021

Contents

List of Figures	vi
1 Photodetectors: An introduction to theory and state-of-art of the design approaches	1
1.1 Photodetectors	1
1.1.1 Photodetector structures	3
1.1.2 Optical generation and absorption rates in detectors	6
1.1.3 Photodetectos Parameters	7
1.1.4 Photodetector DC response: Photo current and Dark current	8
1.1.5 Responsivity	9
1.1.6 Photodetector modulation bandwidth	12
1.1.7 From PN photodetectors to PiN photodetectors	14
1.1.8 Waveguide Photodetectors (WPD)	17
1.1.9 Avalanche waveguide photodetectors	19
1.2 State-of-art of GeSi PiN waveguide photodetectors and design approaches	22
1.2.1 Modifying the PD geometries	23
1.2.2 Exploiting Optimized distributed bragg reflectors (DBR) loaction in the WPDs	25
1.2.3 Exploiting photonic band gap crystals	27
1.2.4 Si-LPiN based photodetectors	28
1.2.5 Germanium wrap-around solution and changing the waveguide (coupler) position	32

1.2.6	WPDs with different vertical position of the waveguide . . .	33
1.2.7	Exploiting advanced metallization technologies for contacts	34
1.2.8	Dual injection Ge-on-Si waveguide photodetectors	35
1.2.9	Exploiting plasmonic effect in WPD performance enhance- ment	37
1.3	Summary	39
1.4	State-of-art of the design approaches of waveguide avalanche pho- t detectors	40
1.4.1	State Key Laboratory design, 2016	41
1.4.2	Avalanche photodetectors utilising Ge graded layer	42
1.4.3	Tunneling avalanche phot detectors (TAPD)	43
1.4.4	separated vertical Ge absorption, lateral Si charge and mul- tiplication APDs	44
1.4.5	Lateral Si-Ge-Si p-i-n hetero-junctions APDs	45
2	Models for carriers transport and FDTD method	48
2.1	Physics and properties of semiconductors	48
2.1.1	Energy bands	49
2.1.2	Carrier concentration	50
2.1.3	Carrier transport parameters	54
2.2	Basic equations for Semiconductor-Device operation	55
2.2.1	Maxwell equations for homogeneous and isotropic materials	55
2.2.2	Current density equations	57
2.2.3	Continuity equations	58
2.3	Finite Difference Time Domain formulation (FDTD)	59
2.3.1	Dispersion less Yee implantation of 1D FDTD	62
2.3.2	Stability criterion	65
2.3.3	Material losses	65
2.3.4	Boundary conditions in 1D - Absorbing boundary condition	66
2.4	Multiphysics and numerical simulations of semiconductor devices	67
2.4.1	Structure Generation	67
2.4.2	Optical simulation	67
2.4.3	Electrical Simulation	68

3 Ge-on-Si mode evolution PiN waveguide photodetectors	70
3.1 Design parameters and geometry	71
3.2 Simulation and analysis approach	75
3.3 Simulation results- Butt-coupled waveguide photodetector	77
3.4 Mode Evolution waveguide photodetectors simulation results . . .	79
3.5 Conclusion	82
Bibliography	90

Introduction

The photodetector is the essential device in the front end of an optical receiver that converts the incoming optical signal into an electrical signal in communication systems, known as O/E converter. Semiconductor photodetectors are the prevalent types of photodetectors used in optical communication systems because of their small size, fast detection speed, and high detection efficiency. Similar to the structures of diodes, photodiodes are also based on the PN junctions. However, unlike a laser diode in which the PN junction is forward biased, the PN junction of a photodetector is reversely biased so that only a very small reverse saturation current flows through the diode without an input optical signal. Although the basic structure of a photodiode can be a simple PN junction, practical photodiodes can have various device structures to enhance quantum efficiency. For example, the popular PIN structure has an intrinsic layer sandwiched between the p- and n-type layers, and that is why a semiconductor photodetector is also known as a PIN diode. An avalanche photodiode (APD) is another type of often used detector that can introduce significant photon amplification through avalanche gain when the bias voltage is high enough.

The need for detectors with higher speed is more obvious these days since great advancements have been made in SiPh technologies and communication systems. To this end, many structures have been proposed for this goal. One of the many quantities that make those devices different from each other is the position of the Si waveguide since we have some major drawbacks in different coupling methods such as having a large amount of mismatch between the silicon bus waveguide and Ge-on-Si structure and having a significant absorption

of the incident light in the first few micrometer of the detector as well as considerable amount of coupling loss and power reflection. The mentioned issues can lead to major problems such as saturation in DC and compression in RF current generation under high power illumination, in other words, the cut-off frequency and bandwidth of the device deteriorates as the power of the incident light increases and this makes the PD to have a slow response.

This thesis is dedicated to tackle the above issues and address the challenges we face when designing the PDs. Many solutions have been proposed by different research groups, one of them is to re-engineer the device with respect to the structure and position of the waveguide (coupler) so we can reach more effective illumination of the germanium region of a single waveguide-coupled photodetector approach. This can be done by using Si side coupled waveguide and this results in transferring the light from silicon waveguide into the detector gradually and effectively and eliminates the modal interference that causes the absorption peak and lead to have a uniform absorption throughout the device. Another advantage of the approach which can be addressed is that this method makes the device more broadband and it has a better response in high power illuminations in comparison of its counterparts. This method initially introduced by *Research Laboratory of Electronics, Massachusetts Institute of Technology, USA* in 2017. This thesis is comprised from below chapters each address a challenge in designing the Ge-on-Si PiN waveguide photodetectors and their optimisations:

- The first chapter is dedicated to a brief introduction to the theory of the photodetectors as a specific category of photonic devices and their working principles, fundamentals and their state of art in design approaches introduced so far by different research groups and related figure of merits. We introduce Ge-on-Si PiN waveguide photodetectors and their different structures and the differences comparing to each other. In the second part of this chapter, an introductory theory on **avalanche photodetectors** has been presented followed by state of the art of designing them based on recent research papers that are published.
- In the second chapter of the chapter one we present the details of numerical and multiphysics approaches that commercial tools like *Synopsys Tools* ex-

plot. A 3D finite-difference-time-domain (FDTD) is being adopted to solve the Maxwell's equations for multiphysics simulation of the device. Then the *Sentaurus Device* has been used in order to electrically simulate the device by solving the Poisson drift-diffusion system with a finite-box method based on the Scharfetter-Gummel discretization of the drift-diffusion relations. In addition, the coupling of Maxwell equations and continuity equations to simulate a device has been explained.

- In the third chapter, the numerical and finite-difference-time-domain (FDTD) simulations for O-band and C-Band have been carried out by *Synopsys Tools* for a particular type of Ge-on-Si PIN waveguide photodetectors. Tools such as *Sentaurus Device Editor* have been exploited for defining the geometry of the device, *Synopsys Rsoft FullWave Tool* has been utilized for FDTD simulation of the device to obtain the absorption profile of the devices and at last, *Sentaurus Device* has been utilized to electrical simulation of the device to obtain the dark current, photo current, responsivity and electrooptical response of the device. Moreover, the intensive comparison have been made with its butt-coupled Ge-on-Si PIN waveguide photodetectors counterpart to see the merits of the proposed structure with respect to the their corresponding optical generation rates, Frequency response, dark and photo current and responsivity. In addition to adding strain to the Ge layer has been studied for both structures. The results of these simulations campaigns are supporting prototyping iterations carried out by an industrial partner (Cisco Systems).

Symbol list

- PD , Photodetector,
- WPD , Waveguide photodetector,
- \mathcal{R} , Responsivity,
- q , electron charge,
- h , Plank's constant,
- k_B , Boltzmann's constant,
- E_g , energy gap of the band structure describing a semiconductor,
- T , temperature expressed in K,
- n , electrons density, expressed in cm^{-3} ,
- p , holes density, expressed in cm^{-3} ,
- N_c , conduction band density of states, expressed in cm^{-3} ,
- N_v , valence band density of states, expressed in cm^{-3} ,
- E_c , energy level corresponding to the minimum of the conduction band,
- E_v , energy level corresponding to the maximum of the valence band
- m^* , effective mass of a particle
- $E_{F,i}$, the Fermi level for an intrinsic semiconductor
- E_F , the Fermi level
- E_{ph} , energy of a photon
- φ , electrostatic potential
- U_0 , free space energy in a semiconductor
- G_o , optical generation rate

- $G_{n,p}$, generation rate in the mathematical model for electrons or holes respectively
- $R_{n,p}$, recombination rate in the mathematical model for electrons or holes respectively
- ω , angular velocity of the modulated optical signal, with corresponding frequency $f = \omega/(2\pi)$

List of Figures

1.1	Structures of (a) Photoresist, (b) PN Photodetector and (c) PiN Photodetector	3
1.2	Simplified functional scheme of waveguide photodetectors (WPDs)	4
1.3	Absorption coefficient of some direct and indirect band gap materials being use in photodetectors	5
1.4	Block diagram of photodetector	6
1.5	Simple scheme of detectors	8
1.6	Detector's current	8
1.7	Behaviour of the responsivity compared to the absorption coefficient	11
1.8	Behaviour of the complex responsivity responsivity [16]	13
1.9	Behaviour of the complex responsivity responsivity	13
1.10	The structure of the PN photodetector	14
1.11	Frequency reponse of the PN photodetectors	15
1.12	PiN photodetector's structure	16
1.13	Simplified waveguide photodetector's scheme	18
1.14	Scheme of a conventional avalanche photodetectors [16]	19
1.15	Scheme of a Separated absorption and multiplication avalanche photodetectors (SAM-APDs) [16]	20
1.16	Some issues and related proposed solutions during designing the various PDs.	22
1.17	Simplified model of this approach. [15]	23
1.18	Prototype model of this approach [11]	26
1.19	Prototype model of this approach [28]	27

1.20	Schematic model of this approach proposed by [8]	30
1.21	Schematic model of this approach proposed by [17]	32
1.22	Simplified idea of this approach [9].	34
1.23	schematic diagram of dual injection (a) and its comparison with conventional single injection WPDs (b) [10].	36
1.24	(a): side coupled, (b) : butt coupled and (c) : butt coupling with n-offshoots. [12]	37
1.25	Ag rods on top of i-region in butt coupling structure with n- offshoots, (b) optical generation rate profile along n-i-n direction cut; E-field in iregion of structure (c) without Ag and (d) with Ag. [12]	38
1.26	Summary of the state of the art of the designs	39
1.27	Schematic of the proposed waveguide APD [14]	41
1.28	Band Diagram of the Ge/SiGe/Ge hetrostructure. [20]	43
1.29	Schematic of the design of TAPDs. [25]	44
1.30	Waveguide-integrated Ge/Si SAMC-APD structures introduced herein [18]	45
1.31	Cross-sectional schematics of a waveguide-integrated photodetec- tor with a lateral silicon-germanium-silicon hetero-junction. [5] . . .	46
1.32	CWaveguide-coupled p-i-n photodetector with a lateral silicon- germanium-silicon heterojunction integrated at the end of a silicon-on-insulator waveguide hetero-junction. [4]	47
2.1	Electronic band structure of Si, Ge and GaAs obtained by EPM [22]	49
2.2	One-dimensional formulation of the FDTD method and The orien- tations of Hz and Ey [24]	63
2.3	Visual illustration of numerical dependencies in the 1D FDTD method, squares represent Ey field and circles represent Hz field. [24]	64
2.4	Illustration of the CFL condition. For the parameters chosen within the dashed lines, the propagation is stable (left figure) and becomes unstable (right figure.) [24]	65
2.5	Simulation flow performed by sentaurus	68

2.6	Flowchart of the numerical newton method to solve the Poisson equation along with the continuity equations for electron and holes based on the generation rates obtained by previous step (FDTD simulation)	69
3.1	Our model for Butt-coupled structure	71
3.2	Our model for Mode evolution structure	72
3.3	giving some names and parameters	72
3.4	giving some names and parameters	73
3.5	Mode evolution WPD design parameters	73
3.6	Optical generation rate in linear(right) and logarithmic(left) scale for butt coupled structure	77
3.7	PI curve of the butt coupled WPD	78
3.8	Frequency response of the butt coupled WPD	78
3.9	Optical generation rate in linear(right) and logarithmic(left) scale for Mode evolution structure	79
3.10	PI curve of the Mode evolution WPD	80
3.11	Frequency response and cut off frequency of Mode evolution structure	80
3.12	Optical generation rates in Log scale	82
3.13	Cut of frequency for all cases	83
3.14	Responsivity for the all cases	84

Photodetectors: An introduction to theory and state-of-art of the design approaches

1.1 Photodetectors

Photodetectors are one of the most common types of optoelectronic technology in use today. Examples range from the simple devices that automatically open supermarket doors and respond to TV and video-cassette-recorder (VCR) remote controls to photodiodes in fiberoptic connections, charge-coupled devices (CCDs) in video cameras, sensitive cameras used in medical imaging (see Fig. 1), and enormous arrays used by astronomers to detect radiation from the other side of the universe. Photodetectors are present in a variety of devices used in commerce, industry, entertainment, and research. The field of photodetector design and use has grown to the point that few practitioners have a complete overview.

Photodetectors (PDs) are the first subsystem in the communication system receiver chain. They serve the purpose of conversion an optical (analog or digital) signal into an electrical signal, typically a current (called the photocurrent, i_L). The physical mechanism behind these kind of semiconductor detectors is the optical generation of electron-hole (e-h) pairs through the absorption of incident photons. Photogenerated e-h pairs are then separated and collected to the external circuit by an electric field. Such a collecting field can be induced by an external

voltage bias, typically a reversed bias voltage applied to the device.

In some cases, a third step (after photogeneration and collection) is present: the photocurrent is amplified through external or built-in gain processes (APDs). There are a number of performance metrics, also called figures of merit, by which photodetectors are characterized and compared:

- Spectral response (Frequency Response): The response of a photodetector as a function of photon frequency.
- Quantum efficiency: The number of carriers (electrons or holes) generated per photon.
- Responsivity: The output current divided by total light power falling upon the photodetector
- Noise-equivalent power: The amount of light power needed to generate a signal comparable in size to the noise of the device.
- Detectivity: The square root of the detector area divided by the noise equivalent power.
- Gain: The output current of a photodetector divided by the current directly produced by the photons incident on the detectors, i.e., the built-in current gain.
- Dark current: The current flowing through a photodetector even in the absence of light.
- Response time: The time needed for a photodetector to go from 10% to 90% of final output.
- Noise spectrum: The intrinsic noise voltage or current as a function of frequency. This can be represented in the form of a noise spectral density.
- Nonlinearity: The RF-output is limited by the nonlinearity of the photodetector.

1.1.1 Photodetector structures

According to the working principles of photodetectors, possible semiconductor base detectors can be:

- Bulk detectors like Photoresistors (photoconductors)
- Junction based photodetectors like : PN photodetectors, PiN photodetectors, avalanche photodetectors and photoresistors.

Below, a few possible designs of the PDs have been reported [16]:

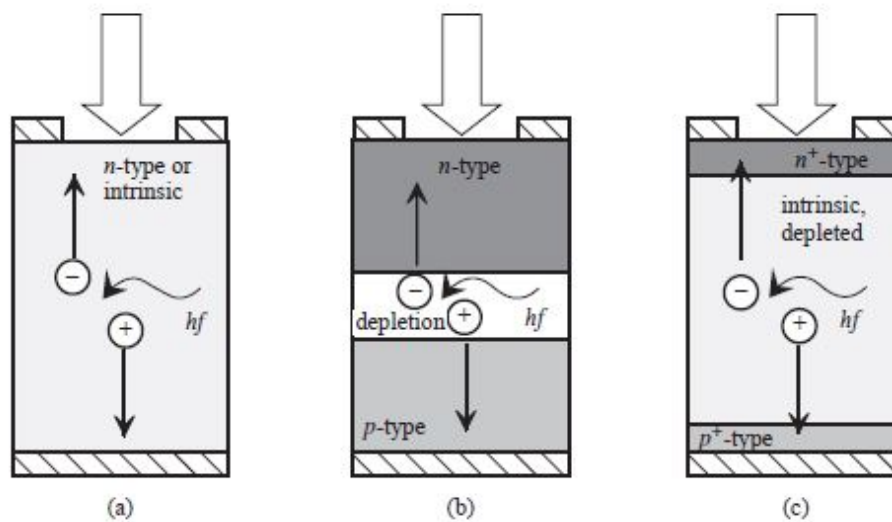


Figure 1.1: Structures of (a) Photoresist, (b) PN Photodetector and (c) PiN Photodetector .

It is clear that the generation of electrons and holes will occur in neutral or depletion region by the incident light and then the generated carriers will be collected by exploiting the reverse bias condition with an anode and cathode on the PD. The scheme of the circuit has been demonstrated as below:

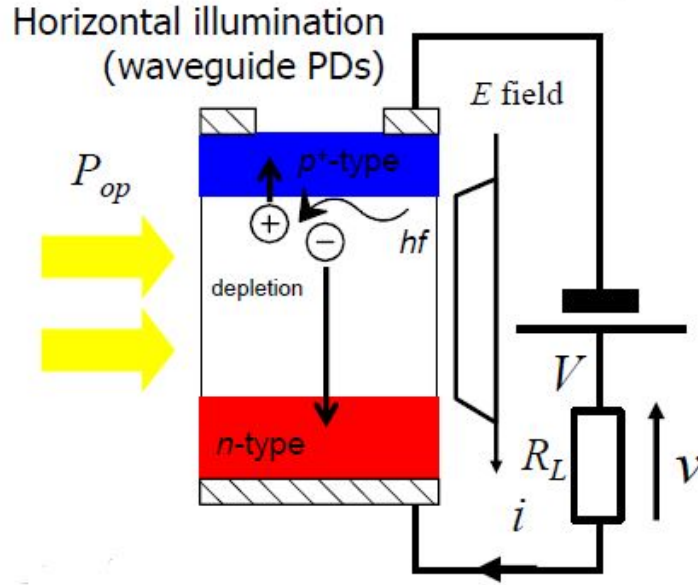


Figure 1.2: Simplified functional scheme of waveguide photodetectors (WPDs)

One may ask about the usage of the reverse bias in the PDs, the reason is obvious, as the width of the depletion or neutral region region is higher, there is more room for light to be absorbed and consequently more carriers will be generated and collected at the end so the photocurrent will be predominant, so the efficiency will be improved, later on, we explain that one of the main motivations behind the fact of turning to the PiN photodetectors rather than PN photodetectors is this phenomena.

Generation of electron and holes (carriers) can be done by illuminating the detector and absorption of the light (its power) according to Fig 1.2. so depending the material we choose for the detectors, there is a absorption threshold which is [16]:

$$E_{ph} > E_g \rightarrow \lambda_{ph} \leq \frac{1.24\mu\text{m}}{E_g\text{eV}} \quad (1.1)$$

we can see that a wide range of the direct band gap materials such as (GaAs, InGaAs, InP , ...) indirect band gap materials such as (Si, Ge) can be used

for detection purposes, but direct band gap materials have higher absorption so this leads to smaller absorption volume and higher speed of PD.

In our own structures the Ge on Si has been exploited for communication systems and light detection, there are clear reasons behind choosing Ge, Ge is a indirect band gap material with two band gap minima, the main one is the lower one which is around 0.66 eV, this minimum can have an impact on transport properties of Ge while the other one which is around 0.9 eV, has an impact on optical properties of Ge and this is the main reason we use Ge for light detection in addition to the fact that it can be used for long-haul communications (high secondary absorption edge due to direct processes and it has a good integration with Si-based photonic ICs. Below, the absorption coefficient of some materials are being used in detectors have been reported [16].

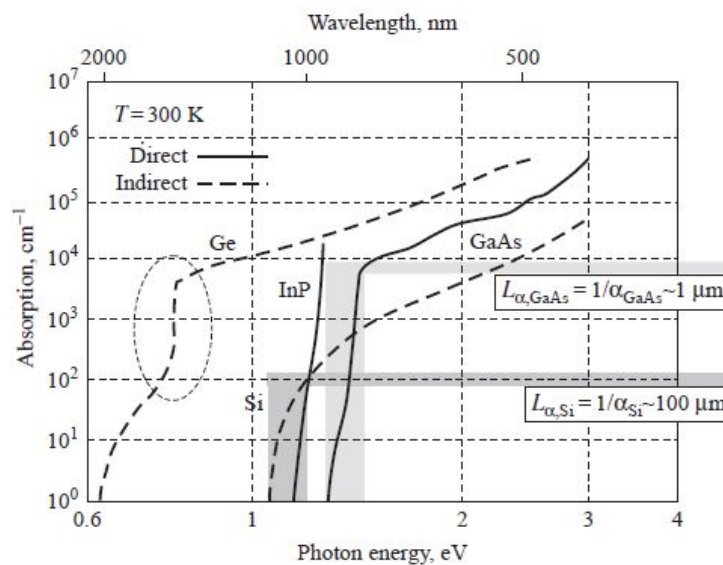


Figure 1.3: Absorption coefficient of some direct and indirect band gap materials being use in photodetectors

The optical power in the absorption region (neutral or depleted region) will decrease exponentially according to below relation:

$$P(x) = P(0)e^{-\alpha x} = P(0)\exp(-x/L_{\alpha}) \quad (1.2)$$

Where L_{α} can be defined as **Absorption length** and α is the absorption coefficient of the material.

Taking a look at the mentioned equations, we can understand that the ab-

sorption region in the photodetectors should be larger and the absorption length which itself depends on the material, so some conclusions could be implied and those are that for direct materials according to 1.3 it would be a few microns and for indirect materials it would be around 10-50 microns which makes the transit time high so leading to slower devices and higher capacitance of the device.

1.1.2 Optical generation and absorption rates in detectors

Optical generation rate or absorption rate is an important parameter which gives us a numerical measurement of absorbing the incident light or generation of the carriers in the absorption region we have in our detector. overall, we can consider our detector like a black box, the incident light will enter the absorption region with the optical power density of P_{op} ($\frac{W}{cm^2}$), then a portion of ΔP_{op} will be absorbed by the detector and the rest of the power will exit the device.

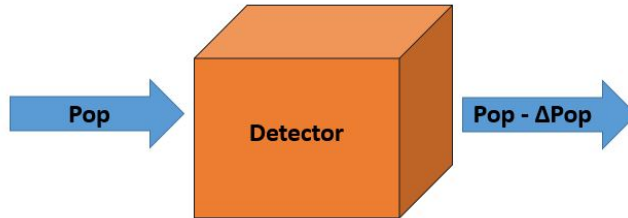


Figure 1.4: Block diagram of photodetector

If we consider the length of the device in 1.4, Δx , the volume of the device can be defined as $V = A\Delta x$ in which A is the surface area of the detector. Now we can write :

$$\frac{dP_{op}}{dx} = -\alpha P_{op} \approx \frac{\Delta P_{op}}{\Delta x} \quad (1.3)$$

Which connects the absorption coefficient. Based on the above equation we can write :

$$\frac{\Delta P_{op}}{\Delta x} = \frac{\text{energy lost due to absorption}}{t \cdot V} = \alpha P_{op} \quad (1.4)$$

$$\frac{\frac{\text{Energy lost}}{t \cdot V}}{\frac{\text{Photon energy } \hbar\omega}{\hbar\omega}} = \frac{\alpha P_{op}}{\hbar\omega} = \frac{\text{Number of photons absorbed}}{t \cdot V} = \frac{\text{Number of carrier pairs generated}}{t \cdot V} = G_{op} \quad (1.5)$$

Where G_{op} stands for the **Optical generation rate**.

Now we can connect the microscopic and macroscopic picture by introducing the expressions for gain, absorption and the optical power per unit surface and we can imply that:

$$\begin{aligned} U_o(\hbar\omega, n, p) &= \rho_{ph} w N_{cv} [f_n f_h - (1 - f_n)(1 - f_h)] + \frac{1}{V} w N_{cv} f_n f_h = \\ &= \bar{g} \rho_{ph} \frac{c_0}{n_r} - \alpha \rho_{ph} \frac{c_0}{n_r} + \frac{1}{V} w N_{cv} f_n f_h = \bar{g} \frac{P_{op}}{\hbar\omega} + \frac{1}{V} w N_{cv} f_n f_h - \alpha \frac{P_{op}}{\hbar\omega} \end{aligned} \quad (1.6)$$

The summation of the first and second term of the right hand side of the equation is equal to radiative stimulated and spontaneous recombination rate (emission) term and the last term is equal to the radiative generation rate or optical generation term. Finally from the variation of power density with x due to absorption we can write :

$$\frac{\alpha P_{op}(x)}{\hbar\omega} = \alpha \Phi_o(x) = G_o(x) = G_o(0) e^{(-x/L_\alpha)} \quad (1.7)$$

This equation conveys a clear message and that is: If the absorption region is shorter than the absorption length, we have lower responsivity and absorption in the PD since most of the input power will leave the device without any absorption.

1.1.3 Photodetector Parameters

There are a multiple number of quantities that we can evaluate the performance of the photodetectors and they are : Photocurrent, Dark current, Responsivity, Electrooptical band width, external and internal quantum efficiency. In this part of the thesis, we dedicate our effort to introduce them and provide a detailed mathematical description for them.

1.1.4 Photodetector DC response: Photo current and Dark current

From electrical view of the functionality of detectors, they are like a one port device, the input is an optical power with the power of $P_{op}(t)$ and with a wavelength of λ and the output of the device is $i_{PD}(t)$ [16].

$$i_{PD}(t) = f\left(p_{op}(t), v_{PD}(t); \frac{d}{dt}, \lambda\right) \quad (1.8)$$

In which, v_{PD} is the detector's bias voltage, λ is the wavelength of the incident optical carrier which affect the absorption coefficient of the material we are exploiting and so the generated carriers in it.

The relationship is typically following a linear trend and saturates for high optical powers. We can write the relation of the detector's current as below:

$$I_{PD}(t) = I_L + I_d = R(\lambda)P_{op}(t) + I_d \quad (1.9)$$

typically we consider the short circuit current according to the blow scheme:

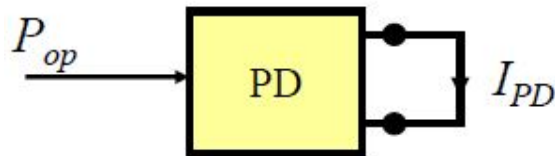


Figure 1.5: Simple scheme of detectors

Looking at equation 1.9, we can see that the current of the photodetectors have a behaviour like:

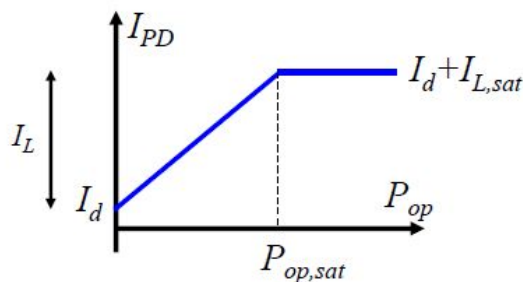


Figure 1.6: Detector's current

I_d stands for the *dark current* of the photodetectors, it is in fact the current in absence of any light, typically its value is around few μA and we want this quantity to be as low as it can be to have a better detector in terms of performance.

I_L stands for *photo current* and it is one of the important parameters that we consider during the detector's comparisons. Their relationship can be defined as below:

$$\begin{aligned} i_d &= f\left(0, v_{PD}(t); \frac{d}{dt}, \lambda\right) \\ i_L &= f\left(p_{in}(t), v_{PD}(t); \frac{d}{dt}, \lambda\right) - i_d \end{aligned} \quad (1.10)$$

Finally, R stands for *Responsivity*, we will talk about this quantity in the next parts.

1.1.5 Responsivity

The responsivity can be defined as the ration between the input optical power and photo current, but before we dive into the details, let's devote some time on how to obtain the photocurrent of a detector. photocurrent i_L can be defined as below:

$$I_L = q \int_V G_o(r, P_{in}) d\underline{r} \quad (1.11)$$

where V is the device active volume. Now we can define the responsivity of the device as and it is measured as (A/W):

$$\mathfrak{R} = \frac{I_L}{P_{in}} \quad (1.12)$$

For high input power the responsivity decreases and then the photocurrent saturates due to device-specific intrinsic effects (e.g. space-charge effects); in fact the total photodetector current can also saturate due to the loading conditions.

Based on the above definitions, we can introduce two additional quantity called **Internal Quantum Efficiency (IQE)** and **External Quantum Efficiency (EQE)** and their relationship will be :

$$\eta_Q = \text{IQE} = \frac{\text{generated pairs}}{\text{photons reaching the active region}} \quad (1.13)$$

$$\eta_x = \text{EQE} = \frac{\text{collected pairs}}{\text{incident photons}} = \frac{I_L/q}{P_{op}/\hbar\omega} = \frac{\hbar\omega}{q} R < \eta_Q \quad (1.14)$$

The external quantum efficiency can be improved by introducing internal gain in the detector, for instance, Avalanche Photodetectors. If we consider IQE equals to one, we can derive the responsivity of the device with below relation:

$$R = \frac{q}{\omega} \eta_Q \approx \frac{q}{\omega}, \quad \omega > E_g \quad (1.15)$$

One may ask that why we mentioned this fact that IQE is always greater than EQE, the reasons are:

- Some of the photons are reflected at the PD interface due to dielectric mismatch (power reflectivity!) or, in waveguide detectors, to the imperfect input coupling
- Some of the photons are absorbed but in regions of the device where they do not contribute to useful device current
- photons are reflected at the PD interface due to dielectric mismatch (power reflectivity!) or, in waveguide detectors, to the imperfect input coupling
- Some of the photons cross the PD without being absorbed (if the absorption length is not \gg than the diffusion length)

Below, the typical behaviour of the responsivity against energy comparing to absorption coefficient of the device has been reported:

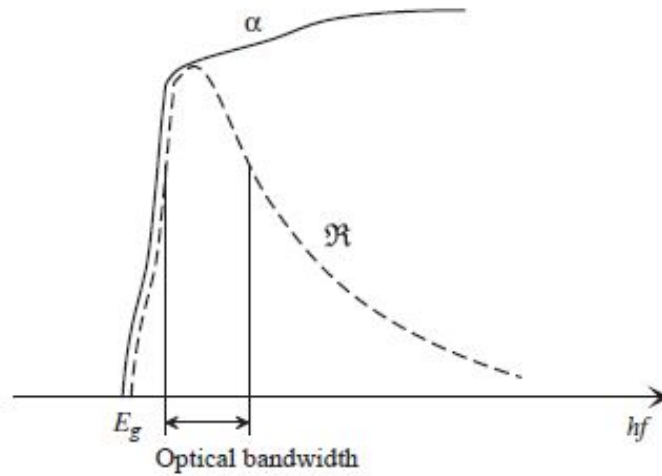


Figure 1.7: Behaviour of the responsivity compared to the absorption coefficient

We can see that for lower energies, the responsivity follows the trend of the absorption coefficient profile and reaches a maximum which is $R_{max} = \frac{q}{E_g} = \frac{1}{E_g[eV]}$ for energies slightly above threshold and for higher energies it will deviated from it and it has a decreasing trend:

$$R = R_{max} \frac{E_g}{E_{ph}} \eta_x \quad (1.16)$$

and there is a clear reason behind the decrease of the responsivity with further increase of the energy of the incident light and that is: After the threshold where $E_{ph} > E_g$, if we increase the input optical power as twice as its initial value, we still have the same electron and hole pair photogenerated, so the photocurrent will be the same while the input optical power has been increased so consequently the responsivity decreases.

In conclusion, Responsivity is one of the most important parameters to be optimised in every design approach we are going to use. it should be improved and the higher it is, the efficient is the photodetector.

1.1.6 Photodetector modulation bandwidth

If we assume that the input optical power and photocurrent have a modulation component with frequency of f_m in addition to the DC term, The first step could be separation of DC and signal component of the photocurrent, input optical power and bias voltage:

$$P_{in} = P_{in,0} + \hat{p}_{in}(t), \quad V_{PD} = V_{PD,0} + \hat{v}_{PD}(t), \quad I_{PD} = I_{PD,0} + \hat{i}_{PD}(t) \quad (1.17)$$

Then we should proceed by writing the phasors related to above components:

$$\hat{p}_{in}(t) = \text{Re} \left(\hat{P}_{in} e^{j\omega t} \right), \quad \hat{v}_{PD}(t) = \text{Re} \left(\hat{V}_{PD} e^{j\omega t} \right), \quad \hat{i}_{PD}(t) = \text{Re} \left(\hat{I}_{PD} e^{j\omega t} \right) \quad (1.18)$$

ω stands for the light frequency, writing the Taylor series around the PD DC working point we can obtain:

$$I_{PD,0} + \hat{i}_{PD}(t) = \underbrace{f(P_{in,0}, V_{PD,0}, 0)}_{I_{PD,0}} + \left. \frac{\partial f(d/dt)}{\partial p_{in}} \right|_0 \hat{p}_{in}(t) + \left. \frac{\partial f(d/dt)}{\partial v_{PD}} \right|_0 \hat{v}_{PD}(t) \quad (1.19)$$

in which the second and third terms are the small-signal photocurrent and dark current, respectively, considering the fact that now we have a relation for the complex responsivity as:

$$\hat{I}_L(f_m) = \Re(f_m) \hat{P}_{op}(f_m) \quad (1.20)$$

Now by utilising the phasors, we can write the small signal relation of the PD current as :

$$\hat{i}_{PD}(t) = \hat{i}_L(t) + \hat{i}_d(t) = \text{Re} \left(\Re(\omega) \hat{P}_{in} e^{j\omega t} \right) + \text{Re} \left(Y_{PD}(\omega) \hat{V}_{PD} e^{j\omega t} \right) \quad (1.21)$$

where Y_{PD} is detector's small signal admittance. then we write :

$$\hat{I}_{PD}(\omega) = Y_{PD}(\omega) \hat{V}_{PD}(\omega) + \hat{I}_L(\omega) \quad (1.22)$$

The *complex responsivity*, describing the detector small-signal frequency response, is typically a low-pass function of the modulation frequency.

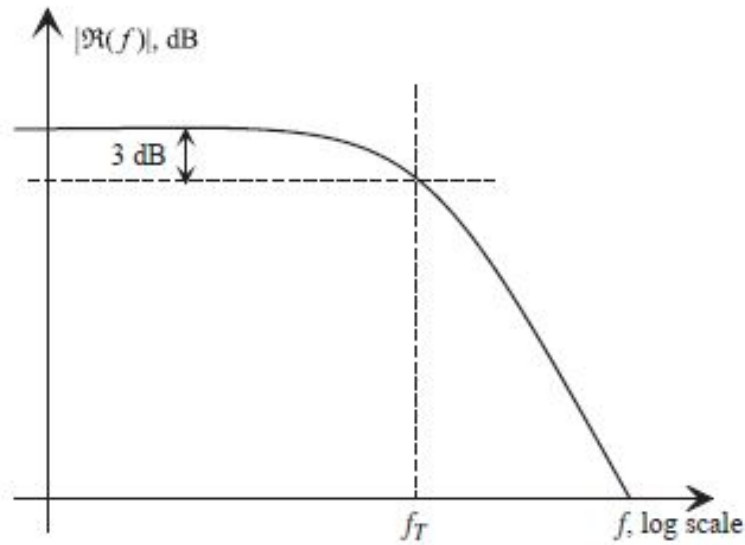


Figure 1.8: Behaviour of the complex responsivity [16]

To discuss the photodetector speed, we should first derive the equivalent circuit for PDs, it can be shown that the equivalent circuit is like below: Now based

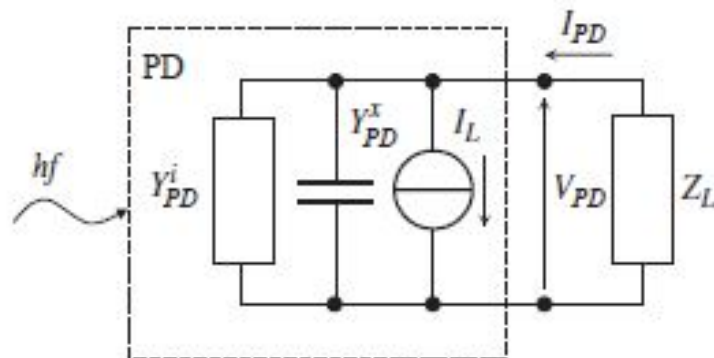


Figure 1.9: Behaviour of the complex responsivity

on what we reported in 1.9 we can see that the main parameters which controls the photodetector speed are **Extrinsic and intrinsic cut off mechanisms**. The intrinsic cut off mechanism can be affected by the minority carrier life times, active region transit time and internal device capacitance (admittances) and extrinsic cut off mechanisms can be affected by the load capacitance and extrinsic parasitic. According to the 1.9 we can write :

$$I_{PD}(\omega) = [Y_{PD}^i(\omega) + Y_{PD}^x(\omega)] V_{PD}(\omega) + I_L(\omega) \quad (1.23)$$

Y_{PD}^i is the detector intrinsic admittance and Y_{PD}^x PD is the detector parasitic (usually capacitive) admittance. Assuming that $Z_L = R_L$ and C_{PD} is the total capacitance of the detector, we can obtain the below relation:

$$I_{R_L}(\omega) = -\frac{I_L(\omega)}{1 + j\omega R_L C_{PD}} \rightarrow |I_{R_L}(\omega)| = \frac{|I_L(\omega)|}{\sqrt{1 + \omega^2 R_L^2 C_{PD}^2}} \quad (1.24)$$

Taking into the account 1.20, we can write :

$$|\mathfrak{R}_i(\omega)| = \frac{\mathfrak{R}}{\sqrt{1 + \omega^2 R_L^2 C_{PD}^2}} \quad (1.25)$$

$$f_{3dB} = \frac{1}{2\pi R_L C_{PD}} \quad (1.26)$$

1.1.7 From PN photodetectors to PiN photodetectors

A pn photodiode can be constructed by putting a highly doped p-type layer on the device surface followed by n-type layer but less doped substrate. this structure has a major disadvantage and that would be Photons are absorbed not only in the (small) depletion region, but also in the (larger) diffusion regions, we can define diffusion length as:

$$L_x = \sqrt{D_x \tau_x} \quad (1.27)$$

for each side of the detector.

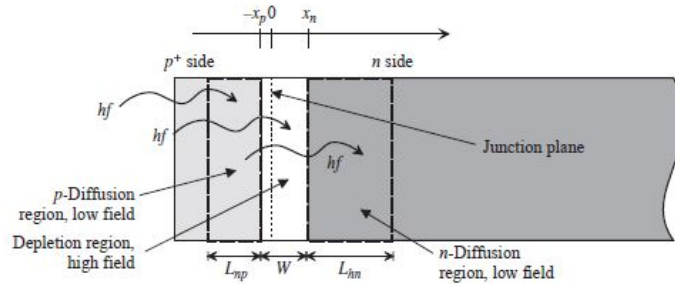


Figure 1.10: The structure of the PN photodetector

And the total current would be :

$$I_L = qA \int_W G_o dx + I_{Lp} + I_{Ln} \approx qAG_o (W + L_{np} + L_{nn}) \quad (1.28)$$

At first glance, we may say that the generated carriers in the diffusion region may increase the responsivity, but small signal frequency domain shows that :

$$I_L(\omega) = qAG_o \left(W + \tilde{L}_{np} + \tilde{L}_{hn} \right), \quad \tilde{L}_{np} = \frac{L_{np}}{\sqrt{1 + j\omega\tau_h}}, \quad \tilde{L}_{hn} = \frac{L_{hn}}{\sqrt{1 + j\omega\tau_n}} \quad (1.29)$$

Finally the additional response will die out with cut off frequency of order of transit time and the whole response has two cut off frequency.

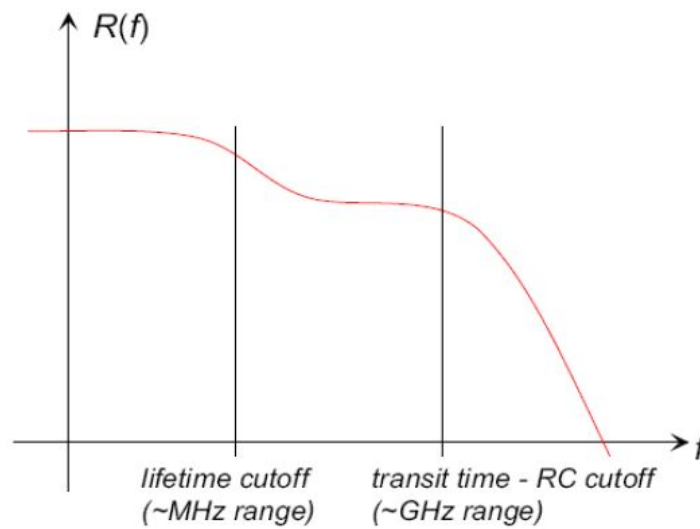


Figure 1.11: Frequency reponse of the PN photodetectors

In order to improve the frequency response and efficiency of the device ,depletion region has to be made larger than the diffusion regions and the absorption length we can either have a really high reverse bias which is unpractical or increase the width of the depletion region. To this aim, we can increase the width of the depletion region with a lightly dope intrinsic material and this will lead us to have **PiN photodetector**.

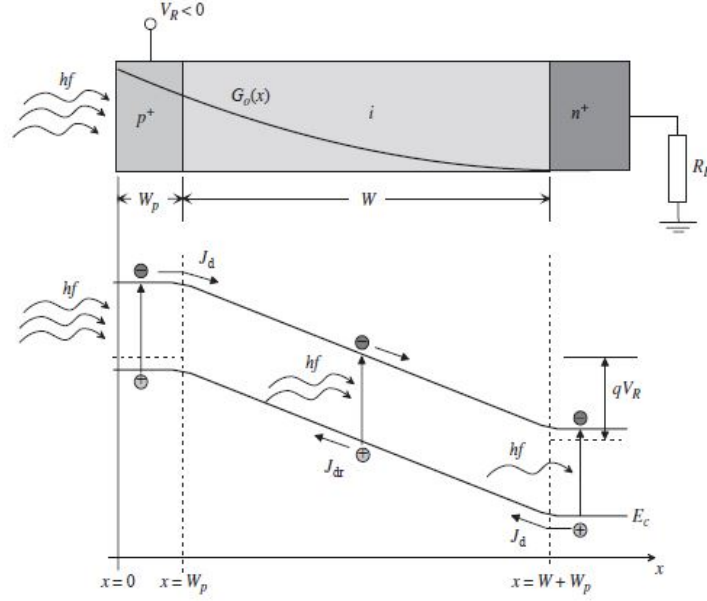


Figure 1.12: PiN photodetector's structure

Exploiting the relation 1.11 we can write the photocurrent of PiN detectors as [16]:

$$I_L = \eta_Q \frac{q}{hf} P_{in} (1 - R) e^{-\alpha W_p} \left(1 - \frac{e^{-\alpha W}}{1 + \alpha L_{hn}} \right) \quad (1.30)$$

From the 1.30 both quantum efficiencies and responsivity can be calculated. Turning to the frequency response of the PiN detectors, there are four main mechanisms which affect the speed of the PiN photodetectors under a dynamic excitation.

- the effect of the total capacitance of the device which has the relation of:

$$C \approx \frac{\epsilon A}{W} \quad (1.31)$$

- the transit time of the carriers across the depletion region, Due to the large absorption region width W the transit time of photogenerated carriers is not negligible, Approximations to the 3dB transit-time limited bandwidth can be derived:

$$f_{tr} \approx 0.44 \frac{v}{W} = 0.44 \frac{1}{\tau_{tr}} \quad (1.32)$$

where v is the electron velocity (large W) or an average effective speed of electrons and holes (small W).

- the diffusion time of carriers generated outside the undepleted regions (mainly in homojunction devices)
- the charge trapping at heterojunctions (in heterojunction devices).

Eventually, the RC limited bandwidth and The total bandwidth can be approximated by:

$$f_{RC} = \frac{1}{2\pi R_L C} \quad (1.33)$$

$$f_{3dB} \approx \frac{1}{\sqrt{\frac{1}{f_{RC}^2} + \frac{1}{f_{tr}^2}}} \quad (1.34)$$

The above relations vehicle a clear message, the frequency response of the PiN PDs is some kind of **speed-efficiency trade-off** since:

$$f_{RC} \propto W, \quad f_{tr} \propto \frac{1}{W}, \quad \eta_x \propto W \quad (1.35)$$

This trade-off will be consider as a minus point in PiN photodetectors and the main motivation of introduction of waveguide photodetectors (WPDs) is elimination of this limit.

1.1.8 Waveguide Photodetectors (WPD)

In waveguide photodiodes, the photon flux and the photocarriers' motion are orthogonal. Light is guided by an optical waveguide made of an intrinsic narrowgap semiconductor layer, sandwiched between two highly doped widegap layers [16]. As we mentioned before, the need of elimination of the speed-efficiency trade-off in photodetectors made researchers to turn their attention to a innovative kind of the photodetectors called **Waveguide PiN photodetectors (WPD)**, other than the aforementioned previlage, there are some other advantages we can mention. below a simplified structure of a waveguide photodetector has been reported:

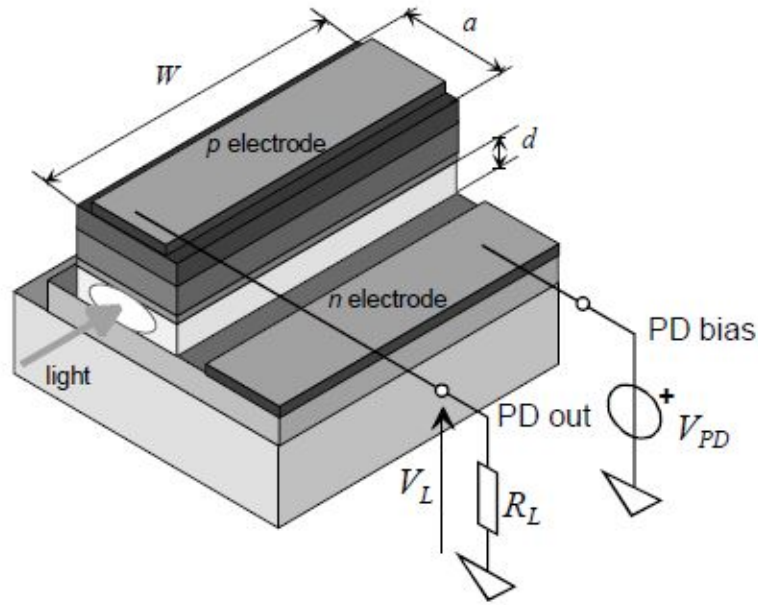


Figure 1.13: Simplified waveguide photodetector's scheme

As we can see, by applying a reverse bias voltage, the photogenerated carriers will be collected by the doped layers with a very short transit time, in addition, we can design the length of the waveguide coupled to the detector long enough so the majority of the photons will be absorbed. W can be made as large as needed to achieve 100% efficiency and since d is small the transit time is not a bottleneck, The capacitance is low despite the small d because of the small a and this fact leads to elimination of the RC limits, The dark current is drastically reduced due to the small Wa , but coupling between the waveguide and detector is a critical factor to be considered in our designs later on. Overall, we can summarise the given information as below:

$$f_{RC} \propto \frac{d}{Wa}, \quad f_{tr} \propto \frac{1}{d}, \quad \eta_x \propto W \quad (1.36)$$

1.1.9 Avalanche waveguide photodetectors

Avalanche photodetectors or (APDs) are a subcategory of photodetectors which utilise the avalanche multiplications by *Impact ionization* mechanism [16] to amplify the photocurrent of the device. This kind of structures offers higher responsivity, higher photocurrent and better sensitivity integrated with higher noise and lower speed. In any APD structure, there are two regions which are included and they are *Generation region* and *Multiplication region*. In conventional APDs the two regions are integrated with each other but recently in order to reduce the noise of the device a new structure based on the conventional APDs has been offered and they are called *SAM-APD* which stands for separated absorption and multiplication avalanche photodetectors, below, the structure of the two devices with their electrical profile have been reported:

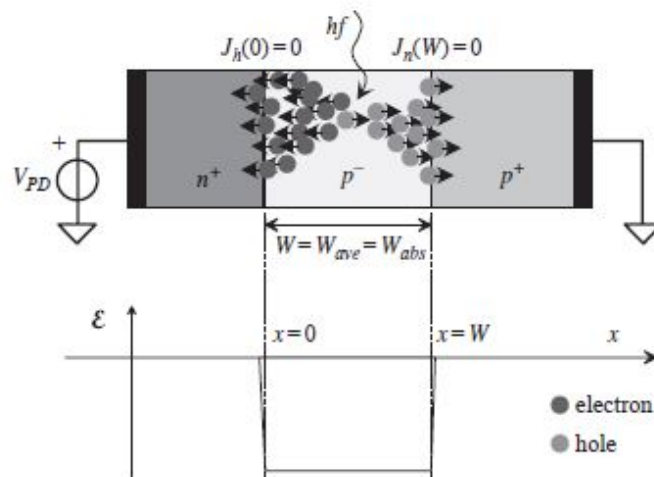


Figure 1.14: Scheme of a conventional avalanche photodetectors [16]

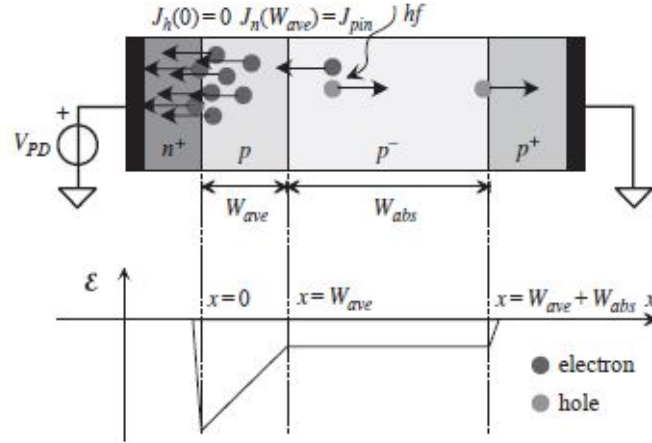


Figure 1.15: Scheme of a Separated absorption and multiplication avalanche photodetectors (SAM-APDs) [16]

Solving continuity equations [16] for APDs we can obtain that the APDs photocurrent is exactly like PiN photodetectors but with a multiplication coefficient known as gain.

$$I_L = M_n I_{pin} = M_n \times q A W_{abs} \alpha \frac{P_{op}}{\hbar \omega} \quad (1.37)$$

In which M_n can be defined as the avalanche ionization coefficient and can be derived as below:

$$M_n = \frac{1}{1 - \int_0^{W_{av}} \alpha(E) e^{-\int_0^x (\alpha(E) - \beta(E)) dx'} dx} \quad (1.38)$$

Or

$$M_n \approx \frac{1}{\left[1 - \left(\frac{V - R_s I}{V_{br}}\right)\right]^n} \quad (1.39)$$

As an empirical expression for APDs ionization coefficient. we can also imply that the responsivity of APDs is higher than PiN photodetectors by the ionization coefficient.

Taking into the account what has been explained so far, we can conclude the APDs as below:

- Turning to the speed of APDs, they are slower than PiN counterparts, the reason is that we should add to the intrinsic transit time the avalanche build-up time and an additional transit time of non-avalanche triggering carriers through the avalanche region and this makes the device slower.

- the noise or current fluctuations is higher than PiN photodetectors and this parameter along with the avalanche build-up time can be minimized if the avalanche coefficients are very different.
- To make a fast and not too noisy device we have however to accept a reduction of avalanche gain typically lower than 10.
- The sensitivity is higher than PiN photodetectors but as it was mentioned before, they have higher noise.

As we proceed, we also introduce some state-of-art of the design for avalanche waveguide photodetectors too.

1.2 State-of-art of GeSi PiN waveguide photodetectors and design approaches

Throughout the history of photodetectors, many research groups along the world devote their efforts to design a fast and optimised waveguide photodetectors. during the design procedures, researchers and engineers encounter various issues in terms of design parameters and they propose various solutions, some of them and their related possible design methods have been demonstrated as below:

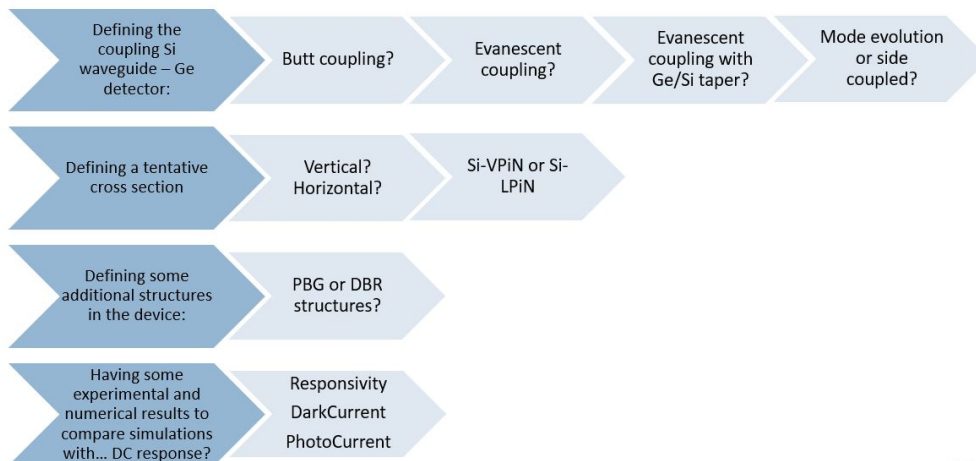


Figure 1.16: Some issues and related proposed solutions during designing the various PDs.

This part of the thesis is dedicated to address each design approaches proposed by different research groups in literature in details, their related effects on the performance of photodetectors and their advantages and disadvantages with respect to our own structures.

1.2.1 Modifying the PD geometries

In 2016, researchers in department of electronics and communications of *University of McGill and Concordia* [15], Proposed an approach in order to enhance the performance of a conventional butt-coupled Ge-on-Si waveguide photodetectors. The method consisted of changing the Ge layer geometries like its width and length and observed the results of these modifications on the PD responsivity, dark current, photocurrent and frequency response. The method then was proceeded by changing the geometry of metallic contacts above Ge in order to reduce the metallic loss, the very same problem that we encountered in our own structure. The simplified scheme of this method has been shown below:

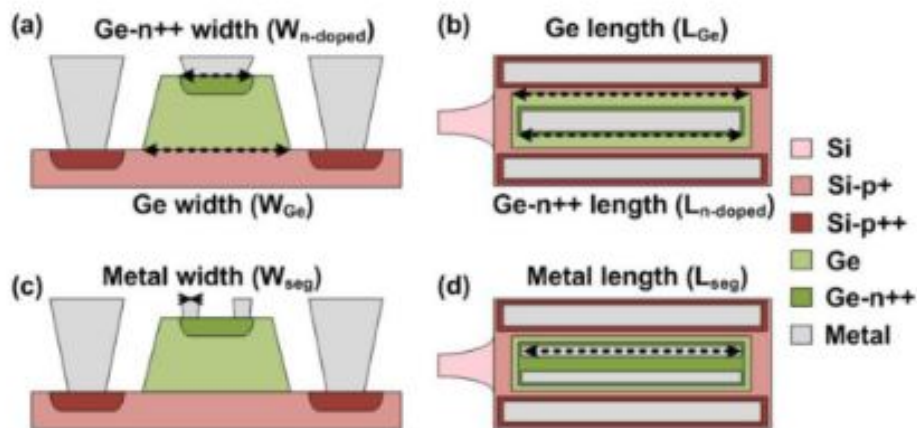


Figure 1.17: Simplified model of this approach. [15]

During this procedure, they realised that an increase in the width of the Ge layer will lead to increase of the dark current and decrease in the bandwidth of the PD while the responsivity remained almost constant, In addition, they demonstrated that with increase of the Ge length, with increase of responsivity of the PD, the PD shows deterioration in the bandwidth and dark current which increased almost linearly with the increase of length. They simulated the structure multiple times but with different contact structures, instead of one centred metallic contact, they used two off-centred contact and the investigated the behaviour of the PD with variation of the gap between contacts, the results were significant increase in the responsivity (greater than 1) and bandwidth and decrease of dark current for two off-centred contact with a gap of $1.6\mu m$ and the width of $1\mu m$. To summerize, they realised that changing the structure of the metallic contacts

above the Ge layer could be the most viable approach in order to enhance the performance of the detectors, Moreover, we could obtain even higher values for the bandwidth by exploiting some additional circuits like gain induced inductors. these final inclusions after this experiment have been obtained:

- Responsivity depends more on the length rather than width so using the optimized length is of importance.
- The results show that a top centered aluminum (Al) contact with a width of 3.6 μm reduces the responsivity by 19% due to metal absorption compared to the simulation result not considering the effect of metal loss.
- the dark current increases linearly with Ge area.
- Although the junction capacitor of the p-i-n PD decreases with reduced size, the smaller width of the n doped Ge area leads to larger series resistance reducing the bandwidth of the PD.
- The linear increase of the measured dark current (green line) with the length of the photodetector shows the dominance of the bulk current.
- It seems as we increase the gap between metal contact on top of Ge could increase the responsivity.

1.2.2 Exploiting Optimized distributed bragg reflectors (DBR) location in the WPDs

In 2017, researchers in *State Key Laboratory of Advanced Optical Communication Systems and Networks, University of Peking* in China, Proposed an interesting way in order to hinder the light escape from Ge layer [11]. As we can see later, one of the major problems leads to decay in responsivity is the fact that the electromagnetic light will not be absorbed at first try when the device is illuminated, this problem is more obvious in the wavelengths near 1550 nm, so they proposed a solution and that was exploiting a distributed bragg reflector or DBR in an optimised location in order to prevent the ligh to escape and prepare it for second absorption. The location and the trenches width should be optimized in order to have maximum reflection and maximum response. The DBR is located at the end of the silicon waveguide in conventional butt-coupled structure. In [11] it was explained that The DBR structure in this case was constructed by etching 220 nm deep trenches on the SOI over the course of 10 cycle for all cases.in this particular case, the DBR showed the reflectivity of 98.7 % at 1550 nm incident light and then the responsivity of the PD was measured for different absorption lengths of Ge layer at the reverse bias of $-1V$. The reason of this modification is that since the unbound light signal oscillates between silicon layers and Ge so we can add the DBR location after the device on the silicon layer.

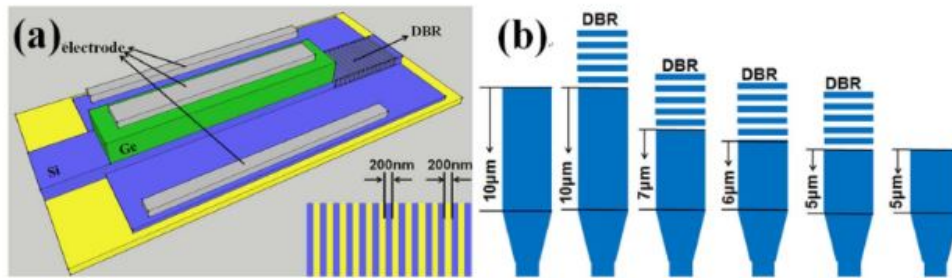


Figure 1.18: Prototype model of this approach [11]

According to the results, this approach may cause a lower size of the device with increased BW and Responsivity and reduced dark current, however, this method did not show a significant increase in responsivity and that was originated from non-optimized DBR location so the location of the structure should be optimized. Moreover, a shorter Ge-on-Si photodetector maintaining high responsivity has a larger bandwidth and a smaller dark current by adding a location-optimized DBR. The 5 μm long photodetector with a DBR shows good performance, with a responsivity of 0.72 A/W, 3 dB bandwidth of 31.7 GHz, and a small dark current of 7 nA at 1550 nm.

1.2.3 Exploiting photonic band gap crystals

Later on in 2018, researchers in *Huawei Technologies Co. LTD* in china proposed a fascinating approach to confine the light in the Ge area. the method was based on utilising photonic band gaps and photonic crystals (PBG and PC) on the Si substrate [28]. In this method, the emphasis was on confining the light in the Ge layer by adding optmise PBG on Si substrate. The main purpose of surrounding photonic crystal is to serve the reflection the outgoing waves back to the Ge absorption regions so that the to-be-wasted power experiences its second absorption and third absorption, However, there is a challenge that we face in terms of optimisation of the PCs and PBGs. One possible solution to this aim could be The structural parameters of the PC are optimized through examining the band diagram of a unit cell of the hexagonal PC slab, which is calculated by the plane-wave expansion method using *BandSOLVE* by *Rsoft Design group*.

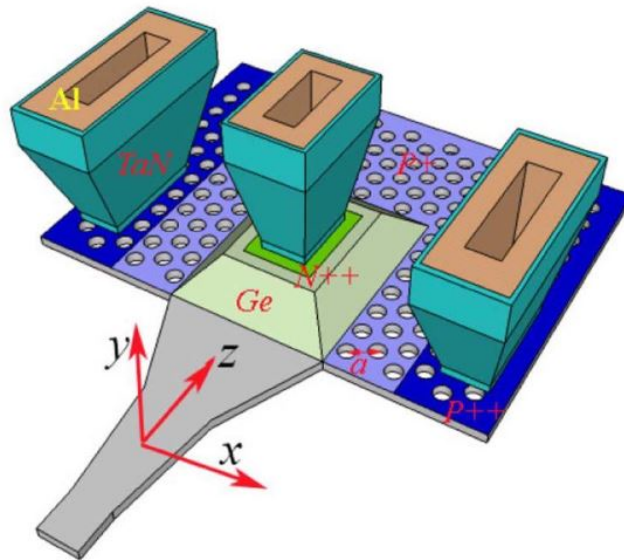


Figure 1.19: Prototype model of this approach [28]

They simulated the conventional BC structure for different lengths of Ge absorption layer and monitored the behaviour of the device. The simulations show a significant enhancement in responsivity of the device at 1550 nm, In addition, they found out that The bandwidth is insensitive to the Ge length though the absorption length decreases from 25 μm to 5 μm . This is reasonable because, as a matter of fact, the RC constant that limits the bandwidth has little dependence on the length of the absorption region as well as the fact that for the PC surrounding case, the missing holes may also increase the series resistance to some extent. This adverse effect may become severe if many columns of PC holes are drilled between the absorption region and the contact regions in addition to challenge we may face in order fabricate the device.

1.2.4 Si-LPiN based photodetectors

The most versatile and promising approach that recently used by many research groups is turning to lateral PiN waveguide photodetectors instead of vertical PiN photodetectors [7] [3] [2]. Many Research groups such as *IMEC*, *CNRS* and *STMicroelectronics* and universities such as *University of Ghent, Belgium* already worked on this concept, proposed Devices and methods and published some papers. Back to the previous section, we explained that the most promising PDs which are currently being used is the ones which are based on a PN or PiN junction at a reverse bias. before introducing lateral solution, most of the conventional PDs including the one which we are going to present in next chapters, were based on a vertical junctions and this design approach would have led us to have a highly doped region on top of Ge layer followed by a metallic contact to satisfy the need of having a enhanced and efficient ohmic contact to collect the electrons induced by illumination. In these novel approaches then the focus is on having a lateral PN or PiN junction instead of a vertical one and this could lead to elimination of the metallic contact losses on top of Ge so the eradication of the metallic loss problem we faced. The chief aim and benefit of this design methodology is since the metal contacts on Ge and free carrier absorption in the doped regions in Ge (for ohmic contacts) are responsible for substantial responsivity decrease we propose a WPD that does not need doping or ohmic contacts on Ge absorbing layer.

This method exploits the lateral double Si/Ge/Si heterojunction, in fact, the intrinsic region of Ge is sandwiched between P- and N-type doped Si regions, located at the end of a Si waveguide then we put both anode and cathode contacts on Si substrate. The method was tested for several design parameters of Ge layer and following results are obtained:

- the optical power is efficiently coupled from the Si waveguide into the Ge area. In addition, the major portion of the optical power is sufficiently confined inside the Ge region, thereby avoiding the light absorption in doped contacts
- the major portion of the optical power is sufficiently confined inside the Ge region, thereby avoiding the light absorption in doped contacts.
- with the increasing width of the Ge region, the optical field confinement of the proposed photodiode structure is enhanced, yielding a comparatively larger portion of optical power inside the Ge region, while the smaller portion of optical power belongs to side regions
- low dark currents were obtained (well below 10 nA at low voltage of 1 V), high photodiode responsivity (up to 1.16 A/W at 1550nm at 1 V), and large 3 dB opto-electrical bandwidths (over 50 GHz).
- The device showed a responsivity as high as 1.16 A/W at low bias voltage of 1 V for the widest and longest device arrangement (i.e. $L_{Ge} = 40 \mu\text{m}$ and $W_{Ge} = 1 \mu\text{m}$). For $L_{Ge} = 10 \mu\text{m}$ and $W_{Ge} = 1 \mu\text{m}$, the device responsivity was about 0.5 A/W. This value is lower than the expected one of 0.63A/W coming from 3D-FDTD simulation
- As we decrease the width and increase the length, the cut off frequency will increase

Later on, researchers at *IMEC Research centre , Belgium* Proposed a new enhanced version of this fundamental modelling in [8]. The major modification with respect to previous approach we just discussed is that the Ge layer is not sandwiched between two junction, they just have contacts with n-type and p-type Si. The simulations performed for different thickness of Ge layer and eventually

these modification resulted in that comparing the experimental S21 curves for a germanium layer thickness of 160 nm and 400 nm (with the same the same germanium width of 500 nm). On the other hand, the modal absorption coefficient is larger for a device with a thicker germanium layer due to the larger modal confinement factor in the germanium layer. Therefore, the Si-LPIN GePD with a 400 nm thick germanium layer has a higher responsivity than that of the device with a 160 nm thick germanium layer (14.2 μm long) so we can conclude that germanium layer thickness can be designed to optimize the opto-electrical bandwidth or responsivity performance of a Si-LPIN GePD device. All in all, A 67 GHz germanium waveguide p-i-n photodetector that has neither doping in nor metal contacts on germanium operating at 1 V is reported. The device was characterized in both the C-band and O-band, showing low dark current and high responsivity. 56 Gbps on-off keying data reception is demonstrated. The opto-electrical 3-dB bandwidth beyond 67 GHz at higher reverse bias should enable even 100 Gbps on-off keying optical receivers.

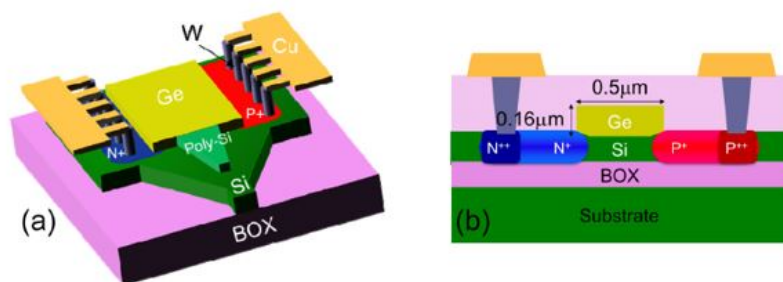


Figure 1.20: Schematic model of this approach proposed by [8]

The recent effort that has been made to enhance this kind of PDs based on lateral junction is proposed by the “CEA-Leti” research lab, France in 2020 [27]. They followed the same concept as we illustrated at the beginning of this section, Ge layer sandwiched between n-type and p-type Si layer, but there is a difference and that is the main focus and goal they have. The aim of this research was to optimise the transit time of the PD since from the literature we know that this quantity is highly dependent on the intrinsic layer, in our case Ge, geometry, Moreover, The Band width of the PD depends on carrier transit time and parasitic capacitance and resistors so In order to properly characterize the dark current of the photo-diodes, designs with different dimensions were implemented with a sweep over width and length and The measurements were held on 27 dies on the wafer to allow a statistical characterization of the devices, then the width of the Ge layer was set 1 μm and 1.4 and they repeated the experiment and they observed that as they increased the width the dark current increased and The latter a linear dependency on the photo-diode length observed while the 1 μm wide photo-diodes did not exhibit the same neat tendency given that the curves represent median values estimated over a statistical sample of 27 dies. The fact of the matter is that the statistics over the small cavity photo-diodes are far less homogeneous compared to the large cavities due to the partial or total stripping of germanium, After this they we swap the width of Ge to see the its effect on the dark current and it was a significant increase. This method was tested on conventional BC PiN WPDs. These structures have been characterized electrically and show a low dark current contribution, i.e 5,8nA at -1V for the standard photo-diode. statistically measured median responsivity of 0,81A/W at -1V and presents a Bit Error Rate of 3×10^{-5} for a 64Gbps NRZ signal.

1.2.5 Germanium wrap-around solution and changing the waveguide (coupler) position

This method, which was proposed at *University of California, Berkeley, Department of Electrical Engineering and Computer Sciences* in 2015 [17] as a modification to the previously mentioned LPiN photodetectors. Other research group tested different geometries such as Ge sandwiched between Si or just having a contact with them, but the major difference of this case with respect to others is that the intrinsic region which is Ge is 'wrapped' around a single mode laterally doped silicon waveguide and germanium will absorb the light from the waveguide evanescently over its length, and by moving the contacts away from the optical mode and this will lead to improvement of quantum efficiency and responsivity of WPD. However, at the end, researchers found out that there is a trade-off naturally for increasing the speed in this model, which is that because the i-Ge region is narrower, the responsivity is reduced. The results also showed the average responsivity values for several devices of a given i-Ge width. However, because of the specific optical mode profile the drop in responsivity is not proportional to the reduction in i-Ge width, and so a trade-off can be made between responsivity and desired bandwidth.

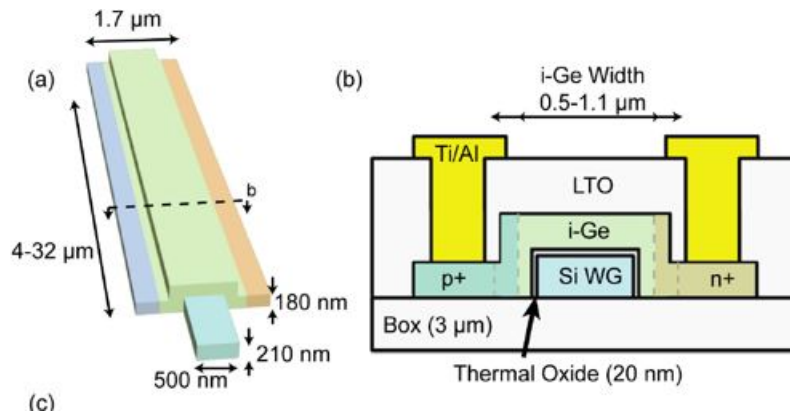


Figure 1.21: Schematic model of this approach proposed by [17]

1.2.6 WPDs with different vertical position of the waveguide

This design approach was proposed by *VTT Technical Research Centre of Finland* in 2020 based on conventional BC PiN waveguide photodetectors [23] and the previous method that was explained in [17] but with a difference and that is the Ge layer is not wrapped around waveguide but they are geometrically matched at the end of the waveguide and beginning of the Ge so the speed of a PiN detector is limited by either the capacitance or the carrier transit time over the i-region (Ge layer). This design which is introduced in [23] has below specifications:

- The sidewalls are doped and therefore the i-region is only about 700nm wide
- There is a 200nm thick silicon slab under the Ge and the incoming silicon waveguide.
- At the Ge PD end of the Si waveguide, the waveguide geometry in Si and Ge waveguides are matched to each other.
- At the other end of the Si waveguide, the waveguide width is $3.0\mu\text{m}$ and the slab thickness is $1.5\mu\text{m}$ and the tapering of the Si waveguide has been designed so that an adiabatic mode field conversion is ensured

Eventually, the simulation results showed that having at least 90% of absorption of the incoming light at the wavelength of 1550nm we need 9 μm length Ge and in order to achieve a fast detector the capacitance must be minimized so the detector length should be as short as possible. The responsivity is about 1 A/W over a large range of optical input power at 1550 nm and as it was seen from the results, the photocurrent did not increase with the increasing bias, which suggested that the carrier lifetimes were high.

To recapitulate, According to previously done research works we can see that an enhancement in the device parameters can be achieved with the lowest cost and modifications in Si-LPIN based photodetectors as well as modifying the contact sets could help to mitigate the metallic loss and responsivity reduction effect due to metal, we can also use rectangle pillars instead of one metal above Ge layer.

Using the DBR structure did not show a significant enhancement in the photodetector performance and it doesn't look promising with the Ge length above 20 um so it is not a good choice while PBG could be helpful after all in the size reduction of the device for integrated photonic circuits.

1.2.7 Exploiting advanced metallization technologies for contacts

This method is the most recent method which is proposed in 2020 by *1Department of Electronic Engineering, Gachon University, Korea*, this approach mostly concerns about BEOL of the process and methods to be used to enhance the responsivity of the photodetectors. a simplified scheme of the method has been shown below [9]:

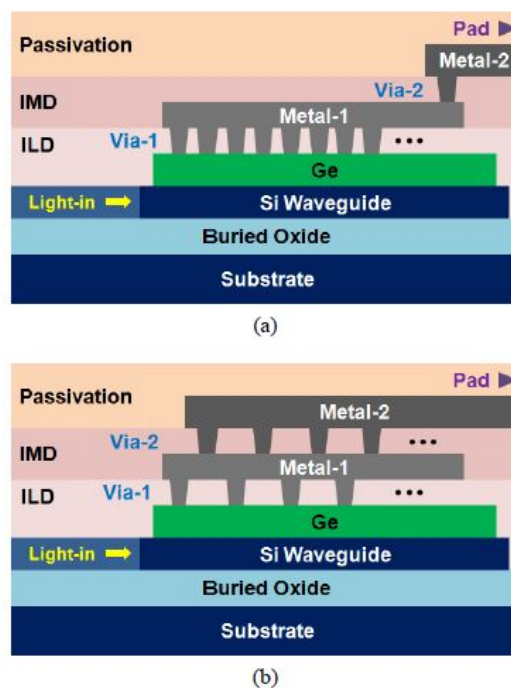


Figure 1.22: Simplified idea of this approach [9].

Three kind of structures depending on the number of vias in each metallic layer in cathod, anode and metal-2 have been simulated at the 1550 nm wavelength : *BMC* which stands for bulk metallic contact which is the conventional type of the contact we had before in the butt-coupled and mode-evolution structures, *SLC*: single layer contact which is described by connecting the anode and cathode to the metal-1 by 42 and 17 pillar vias respectively and lastly *DLC*: doubled layer contact which is described by connecting the *Si* and *Ge* active regions to the metal-1 contacts by 22 and 9 pillar vias respectively and connecting the metal-1 to metal-2 by 20 and 8 pillar vias respectively. at the end the results were interesting, Under the reversed bias voltage of 1V, the dark current for SLC and DLC were significantly lower compared to BMC while the photocurrent corresponding to the DLC was highest followed by SLC and BMC and eventually, turning to the responsivity, the highest one (around 0.75 A/W) corresponded to the DLC followed by SLC and BMC, it should be mentioned that the enhancement in responsivity was not significant but overall, we can conclude that as we increase the number of the pillars (small contacts) on the active regions and the more accessible the metallic contacts, it will lead to plummeting of dark current followed by the enhancement in the responsivity.

1.2.8 Dual injection Ge-on-Si waveguide photodetectors

One possible solution to achieve a high saturation power is to optimise and manipulate the light field distribution as it was indicated in [10] and proposed by *School of Information Engineering, Sanming University, China*.

A schematic diagram of approach and its comparison with conventional single injection WPDs has been depicted below, we can see that the waveguide structure, the incident light is split into two beams by a 3 dB beam splitter and transmits to the photodetection region from both ends.

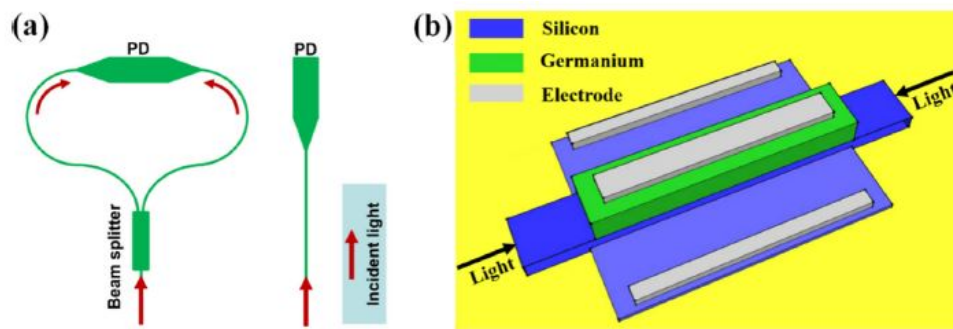


Figure 1.23: schematic diagram of dual injection (a) and its comparison with conventional single injection WPDs (b) [10].

Based on the light transmission characteristics, the light injected from one end would distribute periodically in the germanium absorption layer. An optimum absorption length is obtained depends on the light field distribution.

The FDTD simulation of these kind of devices showed that:

- The responsivity of the 6 μm photodetector is 1.07 A/W and 1.13 A/W for the 10 μm length device at first stage. Although a 6 μm photodetector has a larger light field distribution area, its responsivity at lower incident light power is lower than 10 μm length device
- When the incident optical power exceeds the saturation optical power of the first stage, the responsivity decreases with the increasing incident optical power.
- Turinin to the BW, the 6 μm device showed higher 3 dB cut off frequency in both high saturation input optical power and low optical power in comparison with the 10 μm device.
- Dark current registered higher values for the 10 μm device comparing with the 6 μm device.

Overall, this approach showed the shorter photodetector could get better saturation performance at 1550 nm input wavelength (C-band). When the minimum value of the light intensity from one end is superimposed with the maximum value from the other end, the light intensity distribution is more uniform so a short photodetector with a more uniform light field distribution could have better saturation performance than a longer photodetector therefore optimized dual-

injection Ge-on-Si photodetectors can be more suitable in integrated optical systems in the fields of optical communications, microwave photonics, and optical sensing systems which demand both high efficiency and high speed devices.

1.2.9 Exploiting plasmonic effect in WPD performance enhancement

In 2019 and 2020, *Integrated Systems Laboratory, ETH Zurich* proposed using plasmonic effect to enhance the InGaAs PiN waveguide photodetectors operating at O-band (1310 nm [12] [13]). They proposed three designs for this approach and Below, the schematic designs of their approach has been depicted :

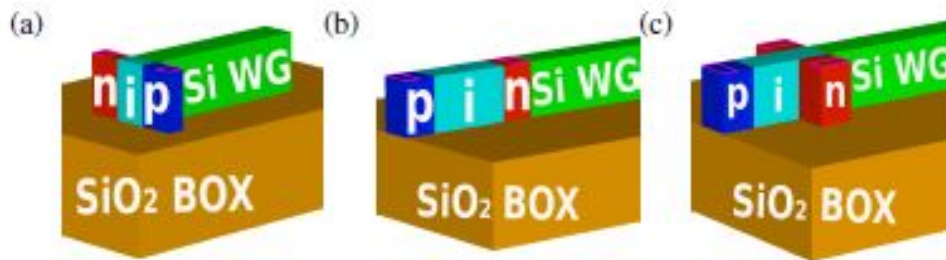


Figure 1.24: (a): side coupled, (b) : butt coupled and (c) : butt coupling with n-offshoots. [12]

Initially, without any plasmonic improvements, butt coupling with n-offshoots showed the best IQE followed by side coupling structure, Turning to optical bandwidth, side coupling structure showed the best response by far and eventually in terms of electrical bandwidth, butt coupling with n-offshoots and butt-coupling without n-offshoots showed the best response. The low optical cut-off frequency of the butt coupling structure with n-offshoots originates from the low electric field in the unbiased i-region between the two n-offshoots. To overcome this drawback, two Ag rods are added on top of the i-region, as it is shown below:

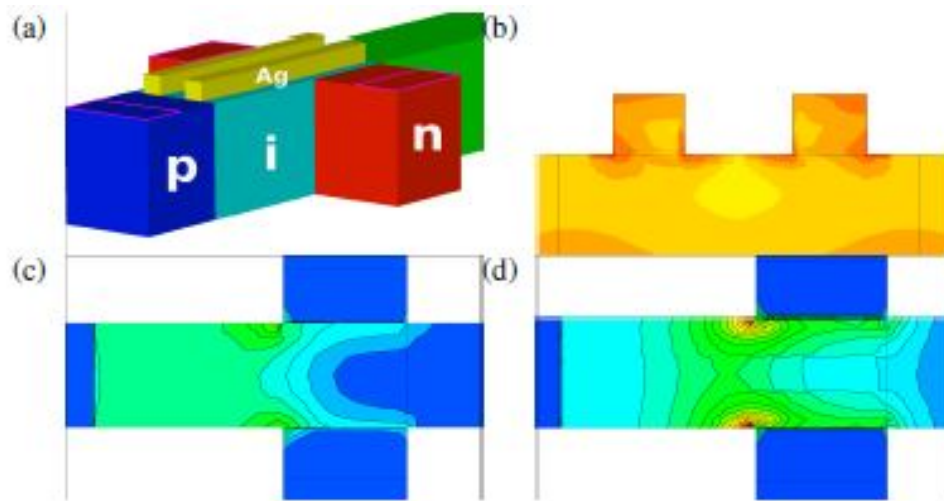


Figure 1.25: Ag rods on top of i-region in butt coupling structure with n-offshoots, (b) optical generation rate profile along n-i-n direction cut; E-field in i-region of structure (c) without Ag and (d) with Ag. [12]

As the metal flattens the potential, the electric field in the unbiased i-region between the two offshoots is significantly improved.

Later on in [13], they investigated the frequency response of this kind of devices and the effect of scaling the geometries. They realised that the plasmonic improvement that applied to the device also enhance the 3dB cut off frequency of the device but the effect of the scaling is important to choose the best and optimised geometry for the device. The lowest cut-off disappears for 500 nm long Ag, while the two higher cut-off frequencies increase without a unique scaling tendency. As the metal stripe gets shorter in length, the field near the intrinsic region and waveguide interface becomes weak again, and thus the lowest cut-off reappears.

Turning to the width of the Ag stripes, two cut-off frequencies showed constraints by drift in the high-field intrinsic region of the non-plasmonic device increase with wider stripe, the minimum width for improvement being 60 nm. This is due to the metal induced field enhancement in the intrinsic region as explained above. However, this enhancement becomes weaker as the stripe becomes narrower so the improvement scales down with stripe width.

And lastly, investigating the thickness of the Ag stripes, scaling the thickness roughly affected the 3dB cut-off frequencies because of the unchanged electric field in the intrinsic region.

1.3 Summary

In this section, the summary of the mentioned approaches has been demonstrated along with some of their advantages and disadvantages they have:

Method	Advantages	Disadvantages
Modifying the PD geometry	<ul style="list-style-type: none"> It is an easy approach to enhance the PD properties 	<ul style="list-style-type: none"> In low scale devices it may be hard to fabricate such devices Scalability problems may come into the action
Exploiting DBR	<ul style="list-style-type: none"> In the small and short devices, it can enhance the device properties We can have second absorption hence increase in responsivity 	<ul style="list-style-type: none"> The position of the DBR should be optimized to have maximum effect The enhancement in parameters is not too much.
Photonic band gap crystals	<ul style="list-style-type: none"> Gives good confinement of light for absorption in Ge layer Increase in responsivity and photocurrent 	<ul style="list-style-type: none"> More complex structure More complicated to simulate Harder to fabricate
Si-LPIN based photodetectors	<ul style="list-style-type: none"> Metallic loss has been eliminated Enhancement in electro optical response Enhancement in responsivity 	<ul style="list-style-type: none"> The characteristic of Si/Ge /Si interface should be defined and investigated. Additional doped region would add additional process steps during fabrication
Germanium wrap-around method	<ul style="list-style-type: none"> Improved quantum efficiency 	<ul style="list-style-type: none"> Trade-off between increasing the speed and geometry of device (bandwidth)
Advanced metallization techniques	<ul style="list-style-type: none"> Reduced dark current No significant difference in responsivity Reduced metallic loss 	<ul style="list-style-type: none"> Complex fabrication process
Dual injection PD	<ul style="list-style-type: none"> Shorter devices we can have Increase in Bw Increase in responsivity 	<ul style="list-style-type: none"> Higher dark current
Exploiting plasmonic effect	<ul style="list-style-type: none"> Enhanced BW Enhanced responsivity Higher speed 	<ul style="list-style-type: none"> Complex to design Expensive to fabricate

Figure 1.26: Summary of the state of the art of the designs

1.4 State-of-art of the design approaches of waveguide avalanche photodetectors

Avalanche photodetectors have been proposed lately as an enhanced version of the PiN waveguide photodetectors since they have higher responsivity and sensitivity but they suffer from some defects such as higher noise and lower speed.

Avalanche photodetectors or (APDs) are widely exploited in fiber-optic communications due to their internal carrier multiplication mechanism, The applications of conventional III–V compound semiconductor APDs are limited because of their low gain-bandwidth products which make them less attractive for high-speed communication [14].

The Ge/Si separate absorption, charge and multiplication (SACM) APDs are considered a promising successor at 1550 nm wavelengths because of the combination of the prominent optical absorption characteristic of Ge and the low- ionization coefficient ratio (which will lead to a low excess noise) property of Si

In this section we introduce some recent state-of-the art of the design of the APDs illustrating the merits and minus points and compare them with each other.

1.4.1 State Key Laboratory design, 2016

In 2016, State Key Laboratory in china propose a design for Waveguide-integrated GeSi heterostructure APDs using a CMOS-compatible process on 8-inch SOI substrate [14]. The structure of the APD was designed as separate-absorption-charge multiplication (SACM) using germanium and silicon as absorption region and multiplication region, respectively. The breakdown voltage (V_b) of such a device is 19 V at reverse bias and dark current appears to be $0.71 \mu\text{A}$ at 90% of the V_b . The device with a $10\text{-}\mu\text{m}$ length and $7\text{-}\mu\text{m}$ width of Ge layer shows a maximum 3-dB bandwidth of 17.8 GHz at the wavelength of 1550 nm. For the device with a $30\text{-}\mu\text{m}$ -length Ge region, gain-bandwidth product achieves 325 GHz [14]

The schematic of the device has been proposed below, they used TaN/Al which was deposited and metalized.

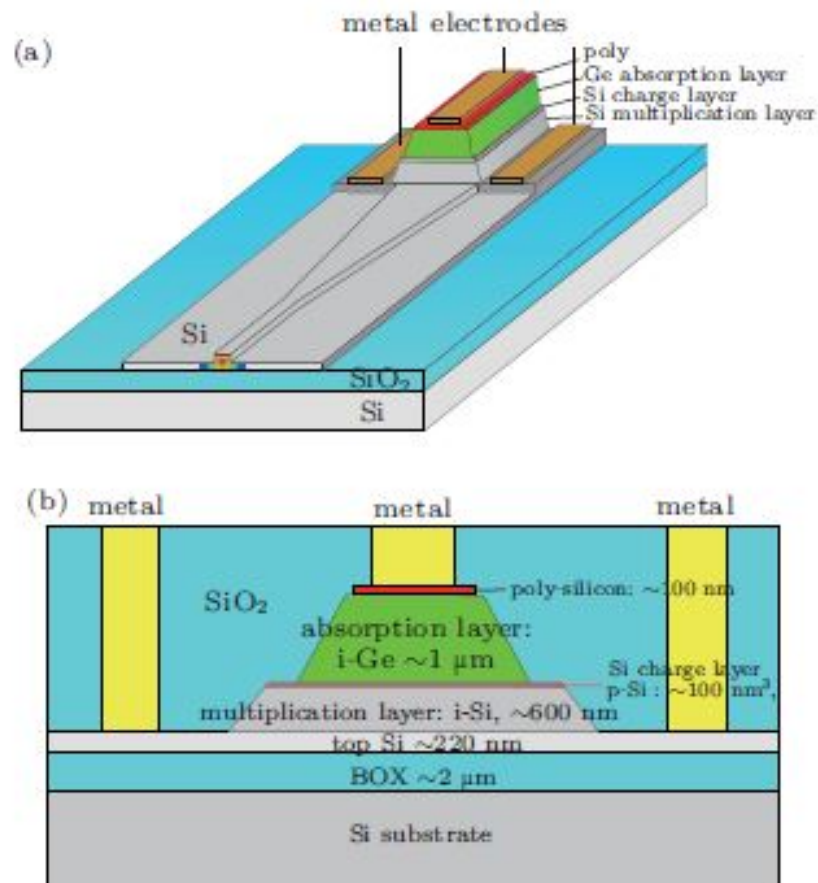


Figure 1.27: Schematic of the proposed waveguide APD [14]

Eventually , The device with a length of $30\text{-}\mu\text{m}$ Ge absorption layer reached a multiplication gain factor of 53 for a C-band communication wavelength of

1550 nm. The maximum 3-dB cut off frequency for the device was 17.8 GHz at a reverse bias voltage of 8 V for the device with 10- μ m-length Ge layer. By considering both optical and RF response, the largest gain-bandwidth product was 325 GHz for the device with 30- μ m-length absorption region under a reverse bias of 18.6 V.

Later on, in 2019 [19] they conducted the precedent of this research to obtain more details on these devices, the results showed enhancement of responsivity and photocurrent with increase in the Ge length, Moreover, It was seen that the optical responsivity decreases gradually as the bias voltage increases however increasing the length of the germanium layer in the photodetectors would increase not only the light absorption but also the junction capacitance, resulting in lower frequency response.

1.4.2 Avalanche photodetectors utilising Ge graded layer

This approach proposed by *NTT Device Technology Laboratories and NTT Nanophotonics Center, Japan* in 2015. This design based on Ge on Si approach, was examined for low voltage and low noise applications, a Ge/graded-SiGe heterostructure is used as the multiplication layer of a separate-absorption-carrier-multiplication structure [20]. This would lead to enhance impact ionization for photo generated holes injected from the Ge optical-absorption layer via the graded SiGe, reflecting the valence band discontinuity at the Ge/SiGe interface. This property will also reduce the operating voltage and enhance the excess noise resulting from the ratio of the ionization coefficients between electrons and holes being far from unity in the waveguide avalanche photodetectors. Below, it has been reported the band diagram of the device in presence of the Ge graded layer, In the n-Ge absorption layer, electron-hole pairs are generated by the direct optical absorption in Ge (wavelengths less than 1.6 μ m), followed by the injection of generated holes into the graded i-SiGe layer without potential barriers

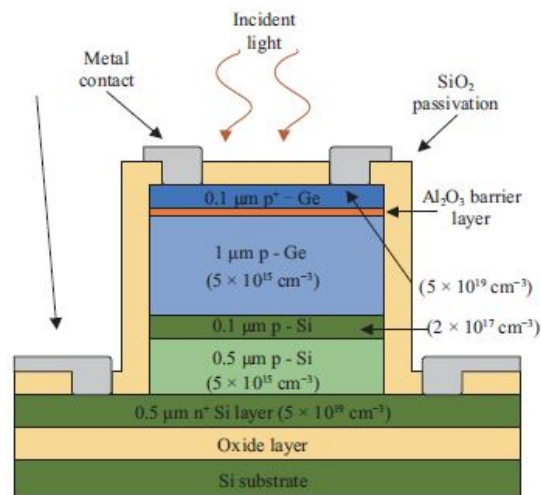


Figure 1.29: Schematic of the design of TAPDs. [25]

Their results show that :

- As the thickness of the barrier layer increases, the photocurrent increases
- As the thickness of the barrier layer increases, the peak gain of the device will undergo a deterioration.

1.4.4 separated vertical Ge absorption, lateral Si charge and multiplication APDs

In 2019, the *School of Information, Beijing University of Technology, Beijing* proposed a design focused on waveguide-coupled Ge/Si separate absorption, charge and multiplication avalanche photodiodes. Their design was of importance since it offered high sensitivity and low noise configuration for optical communications so they presented nanoscale single-mode waveguide-integrated vertical Ge absorption, lateral Si charge and single multiplication configuration for a waveguide Ge/Si SACM APD [18].

Below, the structure of their design has been reported :

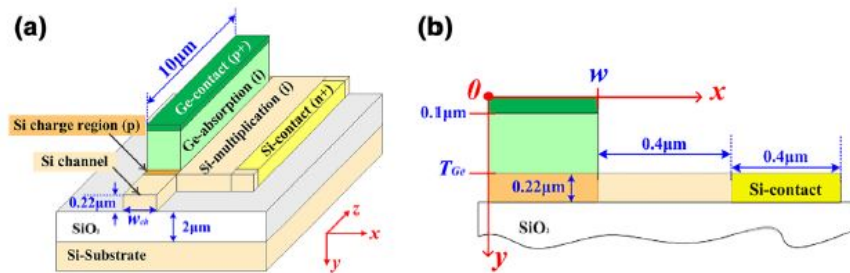


Figure 1.30: Waveguide-integrated Ge/Si SAMC-APD structures introduced herein [18]

Furthermore, their results showed that their device can gain 90% absorption at 1550 nm wavelengths (C-band) with a 10 μm -long Ge absorption layer. The device exhibits a seven times reduction in device length compared to conventional waveguide structures and a 29% increase compared to multi-mode interference coupling. Meanwhile, a 3-dB bandwidth can achieve 47 GHz, which is five times higher than the conventional vertical Ge absorption, lateral Si charge and multiplication APD devices. Moreover, they realised that as the width of the charge layer increases, the absorption in the Ge layer will be enhanced followed by increasing in the absorption efficiency. In addition, they investigated the effect of the charge layer thickness with the BGP (Bandwidth-gain product) and the results showed a significant increase in this parameter with increase of the applied field and the thinner is the charge layer the better is the response of the device.

1.4.5 Lateral Si-Ge-Si p-i-n hetero-junctions APDs

Nowadays, lateral P-i-N photodetectors play a major role in the state-of-art of the design of the waveguide photodetectors, as we introduce in this section lateral Si-Ge-Si p-i-n hetero-junctions APDs proposed by *Centre de Nanosciences et de Nanotechnologies, France* and *University Grenoble Alpes and CEA, LETI, Minattec, France* in 2020 [5]

Below, we can appreciate the proposed structure :



Figure 1.31: Cross-sectional schematics of a waveguide-integrated photodetector with a lateral silicon-germanium-silicon hetero-junction. [5]

Eventually the results showed that :

- The dark current increases with the reverse bias (for a fixed device geometry) and becomes higher when the intrinsic region is less wide (for a fixed bias)
- As the device become larger, the dark current would be increasing and The largest dark-current levels of around 150 nA are found for the largest devices (1 m wide and 40 m long)
- Turning to the responsivity of the device at 1550 nm, for wider and longer devices yield higher levels of photo-responsivity. Under 0 V voltage, the responsivity of heterostructured Si-Ge-Si photodetectors is always low due to the weak built-in electric field
- the responsivity increases with the reverse bias, as a consequence of a higher electric field within the intrinsic Ge zone.
- In terms of the cut off frequency and band width, smaller device registered a higher cut off frequency and as the device geometry increases, the BW decreases. Moreover, it would increase with increase of the applied bias voltage to the device.
- High-Bias avalanche mode , dark and photocurrent , responsivity and the avalanche gain will increase with the increase in the applied voltage and then avalanche collapse is reached at a voltage of about 13.5 V.

Later on, *Université Paris-Saclay, CNRS, Centre de Nanosciences et de Nanotechnologies, France* in 2020, proposed a waveguide-coupled APD based on lateral p-i-n and butt waveguide coupling [4], its schematic view has been reported as below:

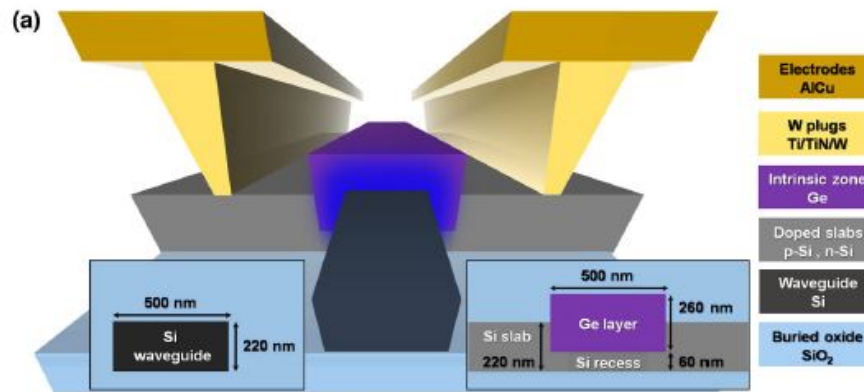


Figure 1.32: CWaveguide-coupled p-i-n photodetector with a lateral silicon-germanium-silicon heterojunction integrated at the end of a silicon-on-insulator waveguide hetero-junction. [4]

They investigated the behaviour of the device with high power input and high reverse bias. They realised as the reverse bias increases, the dark current and photocurrent will be increasing and this was expected, but with increase of the input optical power, the maximum of the avalanche multiplication gain decreased, In addition, with increase of the reverse bias, the responsivity increases until it reaches a maximum value and then it will collapse.

Overall, they reported on a reliable 40 Gbps direct detection of chip-integrated silicon-germanium avalanche p-i-n photo receiver driven with low-bias supplies at 1550 nm wavelength, The photodetector exhibited an internal multiplication gain of 120, a high gain-bandwidth product up to 210 GHz, and a low effective ionization coefficient of almost 0.25. Robust and stable photodetection at 40 Gbps of on-off keying modulation is achieved at low optical input powers, without any need for receiver electronic stages. Such a performance in an on-chip avalanche photodetector is a significant step toward large-scale integrated optoelectronic systems. These achievements are promising for use in data center networks, optical interconnects, or quantum information technologies.

Models for carriers transport and FDTD method

In this section we devote our effort to propose a brief introduction of physics of semiconductors and how they are being handled by synopsys tools and lastly introduction to finite difference time domain (FDTD) for optical and multiphysic simulation of optoelectronic devices. Finally as the last part of this chapter, we investigate the state-of-art of the usage of commercial tools for numerical and multiphysic simulation of semiconductor and optoelectronic devices used by different research groups.

2.1 Physics and properties of semiconductors

Before diving into the details of how commercial tools such as synopsys tools handles the numerical simulation of semiconductor and optoelectronic devices, let's have a brief overview of the physics of semiconductor devices and their principles.

2.1.1 Energy bands

The energy bands are an important characteristics of semiconductors since it defines the transport and optical properties of the materials. Initially the energy bands can be defined as energy-momentum relation of the materials obtained by solving Schrodinger's equation by exploiting the Bloch theorem. 2.1 illustrates the Schrodinger's equation [22].

$$\left[-\frac{\hbar^2}{2m} \nabla^2 + V(\mathbf{r}) \right] \phi_{\mathbf{k}}(\mathbf{r}) = E_{\mathbf{k}} \phi_{\mathbf{k}}(\mathbf{r}) \quad (2.1)$$

Where $V(\mathbf{r})$ is the periodic potential energy with periodicity of the lattice. and The solution of 2.1 have the form of :

$$\phi_{\mathbf{k}}(\mathbf{r}) = e^{j\mathbf{k}\cdot\mathbf{r}} U_n(\mathbf{k}, \mathbf{r}) = \text{Bloch function} \quad (2.2)$$

Which is called the **Bloch function** and $U_n(\mathbf{k}, \mathbf{r})$ is periodic in r with periodicity of the direct lattice and n is the band index and we solve the aforementioned equation for *First Brillouin Zone (FBZ)* of each crystal structure we have which in our case is *Diamond* for *Si* and *Zinceblend* for *Ge* and the band structure of them can be obtained by numerical methods like **Pseudo potential methods** and ***k.p* method**. Below, It is reported the band structures of Si, Ge and GaAs, three versatile materials being used in photodetectors and photonic industry.

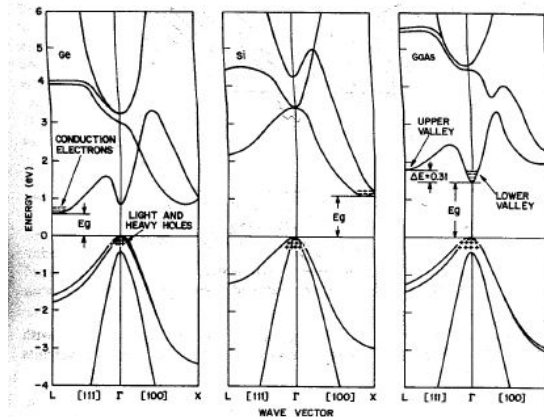


Figure 2.1: Electronic band structure of Si, Ge and GaAs obtained by EPM [22]

The effective mass which is tonsorial with components of m_{ij}^* in conclusion

can be defined as :

$$\frac{1}{m_{ij}^*} = \frac{1}{h^2} \frac{\partial^2 E(\mathbf{k})}{\partial k_i \partial k_j} \quad (2.3)$$

We can see that the effective mass of carriers strictly depends on the curvature of the electronic band in each band and sub-band of the material and as the band is more flat, the effective mass is higher and vice versa.

2.1.2 Carrier concentration

Charge carrier density, also known as carrier concentration, denotes the number of charge carriers in per volume and in SI units, it is measured in m^{-3} . usually carrier concentration is given as a single number, and represents the average carrier density over the whole material. Charge carrier densities involve equations concerning the electrical conductivity and related phenomena like the thermal conductivity. First let's consider the intrinsic case, the number of occupied conduction band levels can be given by [22] :

$$n = \int_{E_c}^{E_{top}} N(E) F(E) dE \quad (2.4)$$

Where E_C is the energy at the bottom of the conduction band and E_{top} is the energy at the top. The density of states at the bottom of the conduction band can be approximated by :

$$N(E) = M_c \frac{\sqrt{2} (E - E_C)^{1/2}}{\pi^2} (m_{de})^{3/2} \quad (2.5)$$

where M_c is the number of the equivalent minima in the conduction band and m_{de} is the density of states of effective mass for electrons and can be given by:

$$m_{de} = (m_1^* m_2^* m_3^*)^{1/3} \quad (2.6)$$

and m_1^*, m_2^*, m_3^* are the effective masses along the principal axes of ellipsoidal energy surfaces. One important function to be used in analysis of semiconductor

is the Fermi-Dirac function which is given as below:

$$F(E) = \frac{1}{1 + e^{\left(\frac{E-E_F}{kT}\right)}} \quad (2.7)$$

Where k is the Boltzmann constant, T is the absolute temperature and E_F is the fermi energy which can be obtained from charge neutrality conditions. The fermi level for intrinsic semiconductors lies very close to the middle of the band gap of the material and in the intrinsic case we have $n = p = n_i$ for carriers concentrations. Eventually 2.4 can be written as:

$$n = N_c \frac{2}{\sqrt{\pi}} F_{1/2} \left(\frac{E_F - E_c}{kT} \right) \quad (2.8)$$

Where N_C stands for effective density of states in the conduction band and can be evaluated as :

$$N_c \equiv 2 \left(\frac{2\pi m_{de} kT}{h^2} \right)^{3/2} M_c \quad (2.9)$$

and $F_{1/2}(\eta_f)$ stands for the fermi-dirac integral. For non-degenerated semiconductors where the fermi level lies between maximum of valance band and minimum of the conduction band, we can write the Boltzmann approximation and write the electron concentrations as :

$$n = N_c e^{\left(-\frac{E_c - E_F}{kT}\right)} \quad (2.10)$$

Similarly we can obtain the same expression for the hole density at the maximum of the valance band and it can be written as:

$$p = N_v \frac{2}{\sqrt{\pi}} F_{1/2} \left(\frac{E_v - E_F}{kT} \right) \quad (2.11)$$

Where N_v is the density of states in the valance band:

$$N_v \equiv 2 \left(\frac{2\pi m_{dh} kT}{h^2} \right)^{3/2} \quad (2.12)$$

where m_{dh} is the effective mass of the holes in the valance band, there is an important note in evaluation of this quantity, we know that the valance band is

anisotropic so m_{dh} can be defined as:

$$m_{dh} = \left(m_{ih}^{*3/2} + m_{hh}^{*3/2} \right)^{2/3} \quad (2.13)$$

and the subscriptions refer to "heavy hole" and "light hole". and again for non-degenerated semiconductors we can write:

$$p = N_v e^{\left(-\frac{E_F - E_v}{kT} \right)} \quad (2.14)$$

introducing all the assets we needed, the fermi level of an intrinsic material can be obtained as :

$$E_F = E_i = \frac{E_C + E_V}{2} + \frac{kT}{2} \ln \left(\frac{N_V}{N_C} \right) = \frac{E_C + E_V}{2} + \frac{3kT}{4} \ln \left(\frac{m_{dh}}{m_d M_c^{2/3}} \right) \quad (2.15)$$

When we **dope** a semiconductor, in fact we introduce some impurity atoms into its crystal structure, impurities can play a role of donors or acceptors, in the case of donor impurity, an electron has been added to the crystal structure for each impurity atom and in case of acceptors, a hole has been added to the crystal for each impurity atom. introduction of impurities in the semiconductors would lead to changes in physical, optical and transport properties of the materials. In this condition, the fermi should adjust itself to preserve global charge neutrality, for the global electric charge neutrality the total negative charge (electrons plus acceptors) must be equal to total positive charge (holes plus donors). Now imagine that we have introduced $N_D (cm^{-3})$ of donors in the semiconductor, we can write :

$$n = N_D^+ + p \quad (2.16)$$

where n is the electron density in the conduction band, p is the hole density in the valance band and N_D^+ is the density of the ionized donor atoms which can be calculated by :

$$N_D^+ = N_D \left[1 - \frac{1}{1 + \frac{1}{g} e^{\left(\frac{E_D - E_F}{kT} \right)}} \right] \quad (2.17)$$

where g is the ground state dependency of the level of the impurity atoms and usually it equals to 2 for donors. the same statement can be written for the accep-

tors :

$$N_A^- = \frac{N_A}{1 + g e^{\left(\frac{E_A - E_F}{kT}\right)}} \quad (2.18)$$

where in this case , g should be equal to 4 since in Ge, Si and GaAs (III-V compounds) each impurity atom is able to accept only one hole with either spin. eventually the global neutrality can be written as :

$$N_c e^{\left(-\frac{E_c - E_F}{kT}\right)} = N_D \frac{1}{1 + 2e^{\left(\frac{E_F - E_D}{kT}\right)}} + N_v e^{\left(\frac{E_V - E_F}{kT}\right)} \quad (2.19)$$

and from this we can calculate all the required concentrations.

Now consider the case where impurity atoms are added, we have a set of equation with which we obtain the carrier concentration in the semiconductor, the first one is :

$$np = n_i^2 = N_c N_v e^{(-E_d/kT)} \quad (2.20)$$

and from the global neutrality we can write :

$$n + N_A = p + N_D \quad (2.21)$$

so now we can write the concentration of the electrons and holes in the n-type semiconductor as:

$$\begin{aligned} n_{n0} &= \frac{1}{2} \left[(N_D - N_A) + \sqrt{(N_D - N_A)^2 + 4n_i^2} \right] \\ &\approx N_D \quad \text{if } |N_D - N_A| \geq n_i \text{ and } N_D \geq N_A \end{aligned} \quad (2.22)$$

and

$$\begin{aligned} p_{n0} &= n_i^2 / n_{n0} = n_i^2 / N_D \\ E_C - E_F &= kT \ln \left(\frac{N_C}{N_D} \right) \\ E_F - E_i &= kT \ln \left(\frac{n_{n0}}{n_i} \right) \end{aligned} \quad (2.23)$$

and for the p-type semiconductor we can write :

$$\begin{aligned} P_{p0} &= \frac{1}{2} \left[(N_A - N_D) + \sqrt{(N_A - N_D)^2 + 4n_i^2} \right] \\ &\approx N_A \quad \text{if } |N_A - N_D| \geq n_i \quad \text{and} \quad N_A \geq N_D \end{aligned} \quad (2.24)$$

$$\begin{aligned}
 n_{po} &= n_1^2/p_{po} \simeq n_i^2/N_A \\
 E_F - E_v &= kT \ln \left(\frac{N_V}{N_A} \right) \\
 E_i - E_F &= kT \ln \left(\frac{p_{po}}{n_i} \right)
 \end{aligned} \tag{2.25}$$

2.1.3 Carrier transport parameters

In this part of this thesis, we introduce some important parameters which is going to be used to numerically simulate the carrier transport in semiconductor devices. The first parameter to be defined is **Mobility**. At low electric fields, the drift velocity v_d , of the carriers, let's say electrons, is proportional to the applied electric field (\mathcal{E}), this proportionality is called mobility and will be expressed with the unit of $(\frac{cm^2}{V-s})$

$$v_d = \mu \mathcal{E} \tag{2.26}$$

Another important parameter which is associated with the mobility is called carrier diffusion coefficient (D_n or D_p).

$$D_n = 2 \left(\frac{kT}{q} \mu_n \right) F_{1/2} \left(\frac{E_F - E_C}{kT} \right) / F_{-1/2} \left(\frac{E_F - E_C}{kT} \right) \tag{2.27}$$

and the same expression holds for D_p and μ_p and $F_{1/2}$ and $F_{-1/2}$ stands for the fermi-dirac integrals and for non-degenerated semiconductors, we can define them as:

$$\begin{aligned}
 D_n &= \left(\frac{kT}{q} \right) \mu_n \\
 D_p &= \left(\frac{kT}{q} \right) \mu_p
 \end{aligned} \tag{2.28}$$

Another important parameter to be mentioned in the carrier transport is the **resistivity**. The resistivity of a semiconductor or ρ can be defined as the proportionality constant between applied electric field to the material and the current density J .

$$\mathcal{E} = \rho J \tag{2.29}$$

and the conductivity can be defined as :

$$\sigma = 1/\rho \tag{2.30}$$

and the relation become:

$$J = \sigma \mathcal{E} \quad (2.31)$$

and for semiconductors for both electrons and holes as the carriers, we can define:

$$\rho = \frac{1}{\sigma} = \frac{1}{q(\mu_n n + \mu_p p)} \quad (2.32)$$

for the n-type semiconductors since $n \gg p$ we can write:

$$\begin{aligned} \rho &= \frac{1}{q\mu_n n} \\ \sigma &\simeq q\mu_n n \end{aligned} \quad (2.33)$$

2.2 Basic equations for Semiconductor-Device operation

There are a number of equations which describe the static and dynamic behaviour of semiconductor devices and they are of importance since many TCAD tools such as *Synopsys tools* uses numerical methods to solve these equations and obtain important parameters [22]. As we proceed we introduce multiple important equations, their role and what we gain by solving them and their role in comparing various devices.

2.2.1 Maxwell equations for homogeneous and isotropic materials

Maxwell's equations are a set of coupled partial differential equations that, together with the Lorentz force law, form the foundation of classical electromagnetism, classical optics, and electric circuits. The equations provide a mathematical model for electric, optical, and radio technologies, such as power generation, electric motors, wireless communication, lenses, radar etc. They describe how electric and magnetic fields are generated by charges, currents, and changes of the fields. The equations are named after the physicist and mathematician James Clerk Maxwell, who, in 1861 and 1862, published an early form of the equations that included the Lorentz force law. Maxwell first used the equations to propose

that light is an electromagnetic phenomenon.

An important consequence of Maxwell's equations is that they demonstrate how fluctuating electric and magnetic fields propagate at a constant speed (c) in a vacuum. Known as electromagnetic radiation, these waves may occur at various wavelengths to produce a spectrum of light from radio waves to gamma rays. The equations have two major variants. The microscopic Maxwell equations have universal applicability but are unwieldy for common calculations. They relate the electric and magnetic fields to total charge and total current, including the complicated charges and currents in materials at the atomic scale. The "macroscopic" Maxwell equations define two new auxiliary fields that describe the large-scale behaviour of matter without having to consider atomic scale charges and quantum phenomena like spins. However, their use requires experimentally determined parameters for a phenomenological description of the electromagnetic response of materials [1].

The equations for isotropic and homogeneous materials can be written as :

$$\nabla \times \mathcal{E} = -\frac{\partial \mathcal{B}}{\partial t} \quad (2.34)$$

$$\nabla \times \mathcal{H} = \frac{\partial \mathcal{D}}{\partial t} + \mathbf{J}_{\text{cond}} = \mathbf{J}_{\text{tot}} \quad (2.35)$$

$$\nabla \cdot \mathcal{D} = \rho(x, y, z) \quad (2.36)$$

$$\nabla \cdot \mathcal{B} = 0 \quad (2.37)$$

$$\mathcal{B} = \mu_0 \mathcal{H} \quad (2.38)$$

$$D(\mathbf{r}, t) = \int_{-\infty}^t \epsilon_s(t-t') \mathcal{E}(\mathbf{r}, t') dt' \quad (2.39)$$

Where 2.39 will be reduced to $\mathcal{D} = \epsilon_s \mathcal{E}$ under static or very low frequency conditions.

- \mathcal{E} : Electric field
- \mathcal{D} : Displacement vector
- \mathcal{H} : Magnetic field
- \mathcal{B} : induction vector
- ϵ_s : Permittivity
- μ_0 : Permeability
- $\rho(x, y, z)$: Total electric charge density
- J_{cond} : Conduction current density
- J_{tot} : Total current density

The 2.36 is **Poisson equation** and it is the most important equation to be considered and solved since it determines the properties of the p-n junction depletion layer that we have in our device.

2.2.2 Current density equations

Current density equation is an important parameter to be obtained since it determines the current flows in the p-n junction of our device, in fact the photocurrent and dark current would be the solution of these equations and these equations will be solved numerically by commercial tools like *Synopsys tools* and specifically *Sentaurus Device*.

$$\begin{aligned} \mathbf{J}_n &= q\mu_n n \mathcal{E} + qD_n \nabla n \\ J_p &= q\mu_p \mathcal{E} p - qD_p \nabla p \\ J_{cond} &= J_n + J_p \end{aligned} \tag{2.40}$$

Where J_p and J_n are the hole and electron current density. if we take a look at the equations, we can see that there are two terms consisting of each equation: the first term is the drift current density which will be caused by the applied electric field and the latter one is the diffusing current density caused by the carrier

concentration gradient in the device. At the low field condition for 1D case, the aforementioned equations can be reduced to :

$$\begin{aligned} J_n &= q\mu_n n \mathcal{E} + qD_n \frac{\partial n}{\partial x} = q\mu_n \left(n \mathcal{E} + \frac{kT}{q} \frac{\partial n}{\partial x} \right) \\ J_p &= q\mu_p p \mathcal{E} - qD_p \frac{\partial p}{\partial x} = q\mu_p \left(p \mathcal{E} - \frac{kT}{q} \frac{\partial p}{\partial x} \right) \end{aligned} \quad (2.41)$$

For the relatively high electric field, the terms $\mu_n n$ and $\mu_p p$ will be replaced by the saturation velocity v_s .

2.2.3 Continuity equations

The most important equations is carrier transport formulation in semiconductor devices, are the continuity equations which describe charge conservation. They can be written as :

$$\begin{aligned} \frac{\partial n}{\partial t} &= G_n - U_n + \frac{1}{q} \nabla \cdot J_n \\ \frac{\partial p}{\partial t} &= G_p - U_p - \frac{1}{q} \nabla \cdot J_p \end{aligned} \quad (2.42)$$

The quantities G_p and G_n are holes and electrons generation rates caused by external excitation such as optical excitation and impact ionization under the high field condition, U_n and U_p are the net recombination rates for electrons and holes respectively. For 1D case and under the low injection condition, those equations can be written as :

$$\begin{aligned} \frac{\partial n_p}{\partial t} &= G_n - \frac{n_p - n_{p0}}{\tau_n} + n_p \mu_n \frac{\partial \mathcal{E}}{\partial x} + \mu_n \mathcal{E} \frac{\partial n_p}{\partial x} + D_n \frac{\partial^2 n_p}{\partial x^2} \\ \frac{\partial p_n}{\partial t} &= G_p - \frac{p_n - p_{n0}}{\tau_p} - p_n \mu_p \frac{\partial \mathcal{E}}{\partial x} - \mu_p \mathcal{E} \frac{\partial p_n}{\partial x} + D_p \frac{\partial^2 p_n}{\partial x^2} \end{aligned} \quad (2.43)$$

The transport models exploited in *Sentaurus Device* differ in the method they use to solve the continuity equations and depending on the device under investigation and the level of the modelling accuracy we need, we can select different transport models such as:

- Drift-Diffusion : Isothermal simulation, suitable for low-power density devices with long active regions.
- Thermodynamic : Accounts for self-heating. Suitable for devices with low thermal exchange, particularly, high-power density devices with long active regions.

- Hydrodynamic : Accounts for energy transport of the carriers. Suitable for devices with small active regions
- Monte Carlo : Solves the Boltzmann equation for a full band structure.

In all of the simulations we performed for our own device, Drif-Diffusion transport model has been used.

2.3 Finite Difference Time Domain formulation (FDTD)

The FDTD method is a rigorous solution to Maxwell's equations and does not have any approximations or theoretical restrictions. This method is widely used as a propagation solution technique in integrated optics, especially in situations where solutions obtained via other methods such as the Beam Propagation Method (BPM) cannot cope with the structure geometry or are not adequate solutions. Since FDTD is a direct solution of Maxwell's curl equations, it therefore includes many more effects than other approximate methods [21]. It is a widely used numerical scheme for approximate description of propagation of electromagnetic waves. It can be used to study such phenomena as pulse propagation in various media. It is a simple scheme and can be mastered relatively fast [24]. The general formulation can be developed by taking into the account the Maxwell's equation we introduced before (2.34 - 2.39), We consider $J = 0$ and $\rho = 0$, we also consider that the devices under investigation comprised by materials that are nonmagnetic meaning that $\mu = \mu_0$. Our journey begins with writing Maxwell's equation and we can consider 3 cases:

- 1D formulation : our medium is infinite in y and z direction and no change in those directions so we can write : $\frac{\partial}{\partial y} = \frac{\partial}{\partial z} = 0$.
- 2D formulation: z direction is infinite and we have no changes in it so : $\frac{\partial}{\partial z} = 0$
- 3D formulation : We have no restriction at all and this case is so computationally expensive.

Now we can write three different formulation for Maxwell equation :

3D formulation:

Since in this case there is no restrictions at all we can write [24] :

$$\begin{aligned} \nabla \times \mathbf{H} &= \begin{vmatrix} a_x & a_y & a_z \\ \frac{\partial}{\partial x} & \frac{\partial}{\partial y} & \frac{\partial}{\partial z} \\ H_x & H_y & H_z \end{vmatrix} \\ &= a_x \left(\frac{\partial H_z}{\partial y} - \frac{\partial H_y}{\partial z} \right) - a_y \left(\frac{\partial H_z}{\partial x} - \frac{\partial H_x}{\partial z} \right) + a_z \left(\frac{\partial H_y}{\partial x} - \frac{\partial H_x}{\partial y} \right) \end{aligned} \quad (2.44)$$

And by exploiting the mentioned expression in the Maxwell's equation, we can obtain:

$$\begin{aligned} \frac{\partial D_x}{\partial t} &= \frac{\partial H_z}{\partial y} - \frac{\partial H_y}{\partial z} \\ -\frac{\partial D_y}{\partial t} &= \frac{\partial H_z}{\partial x} - \frac{\partial H_x}{\partial z} \\ \frac{\partial D_z}{\partial t} &= \frac{\partial H_y}{\partial x} - \frac{\partial H_x}{\partial y} \\ -\mu_0 \frac{\partial H_x}{\partial t} &= \frac{\partial E_z}{\partial y} - \frac{\partial E_y}{\partial z} \\ \mu_0 \frac{\partial H_y}{\partial t} &= \frac{\partial E_z}{\partial x} - \frac{\partial E_x}{\partial z} \\ -\mu_0 \frac{\partial H_z}{\partial t} &= \frac{\partial E_y}{\partial x} - \frac{\partial E_x}{\partial y} \end{aligned} \quad (2.45)$$

Which is the starting point of 3D FDTD implantation being used in the most Tcad tools.

2D formulation:

In case of 2D, based on what we said, since there is no changes in the z direction we can write:

$$\nabla \times \mathbf{H} = \begin{vmatrix} \mathbf{a}_x & \mathbf{a}_y & \mathbf{a}_z \\ \frac{\partial}{\partial x} & \frac{\partial}{\partial y} & 0 \\ H_x & H_y & H_z \end{vmatrix} = a_x \frac{\partial H_z}{\partial y} - a_y \frac{\partial H_z}{\partial x} + a_z \left(\frac{\partial H_y}{\partial x} - \frac{\partial H_x}{\partial y} \right) \quad (2.46)$$

So the Maxwell's equations becomes:

$$\begin{aligned} a_x \frac{\partial H_z}{\partial y} - a_y \frac{\partial H_z}{\partial x} + a_z \left(\frac{\partial H_y}{\partial x} - \frac{\partial H_x}{\partial y} \right) &= a_x \frac{\partial D_x}{\partial t} + a_y \frac{\partial D_y}{\partial t} + a_z \frac{\partial D_z}{\partial t} \\ a_x \frac{\partial E_z}{\partial y} - a_y \frac{\partial E_z}{\partial x} + a_z \left(\frac{\partial E_y}{\partial x} - \frac{\partial E_x}{\partial y} \right) &= -\mu_0 \left(a_x \frac{\partial H_x}{\partial t} + a_y \frac{\partial H_y}{\partial t} + a_z \frac{\partial H_z}{\partial t} \right) \end{aligned} \quad (2.47)$$

We can divide the above formulas into two groups based on the polarisation :
TE and TM

For TE mode we can write:

$$\begin{aligned} \frac{\partial D_x}{\partial t} &= \frac{\partial H_z}{\partial y} \\ \frac{\partial D_y}{\partial t} &= -\frac{\partial E_z}{\partial x} \\ \frac{\partial H_z}{\partial t} &= -\mu_0 \left(\frac{\partial E_y}{\partial x} - \frac{\partial E_x}{\partial y} \right) \end{aligned} \quad (2.48)$$

And for the TM mode we can write :

$$\begin{aligned} \frac{\partial H_x}{\partial t} &= -\frac{1}{\mu_0} \frac{\partial H_z}{\partial y} \\ \frac{\partial H_y}{\partial t} &= \frac{1}{\mu_0} \frac{\partial E_z}{\partial x} \\ \frac{\partial D_z}{\partial t} &= \frac{\partial H_y}{\partial x} - \frac{\partial H_x}{\partial y} \end{aligned} \quad (2.49)$$

1D formulation :

Based on constraints we have, we can write :

$$\nabla \times E = \begin{vmatrix} a_x & a_y & a_z \\ \frac{\partial}{\partial x} & 0 & 0 \\ H_x & H_y & H_z \end{vmatrix} = -a_y \frac{\partial H_z}{\partial x} + a_z \frac{\partial H_y}{\partial x} \quad (2.50)$$

So MW equations become:

$$\begin{aligned} \frac{\partial H_y}{\partial t} &= \frac{1}{\mu_0} \frac{\partial E_z}{\partial x} \\ \frac{\partial D_z}{\partial t} &= \frac{\partial H_y}{\partial x} \end{aligned} \quad (2.51)$$

For **TE** mode and:

$$\begin{aligned}\frac{\partial H_z}{\partial t} &= -\frac{1}{\mu_0} \frac{\partial E_y}{\partial x} \\ \frac{\partial D_y}{\partial t} &= -\frac{\partial H_z}{\partial x}\end{aligned}\tag{2.52}$$

for **TM** mode.

In this chapter, we discuss only the basic implementation of FDTD method in 1D. It is known as the 1D-Yee algorithm since it was first proposed by Yee [26] in 1996 for the 3D case.

2.3.1 Dispersion less Yee implantation of 1D FDTD

We know that for free space we have :

$$D_y = \epsilon_0 E_y\tag{2.53}$$

and the equations can be written as :

$$\begin{aligned}\frac{\partial H_z}{\partial t} &= -\frac{1}{\mu_0} \frac{\partial E_y}{\partial x} \\ \frac{\partial E_y}{\partial t} &= -\frac{1}{\epsilon_0} \frac{\partial H_z}{\partial x}\end{aligned}\tag{2.54}$$

Now we should introduce the *Yee* discretization with the following notation:

$$\begin{aligned}E_y(i \cdot \Delta x, n \cdot \Delta t) &\equiv (E_y)_i^n \\ H_z(i \cdot \Delta x, n \cdot \Delta t) &\equiv (H_z)_i^n\end{aligned}\tag{2.55}$$

Now we use central-difference approximation for space and time derivatives to discretize the 2.54 and eventually They will be second-order accurate in the space and time increments as below:

$$\begin{aligned}\frac{\partial E_y}{\partial x}(i \cdot \Delta x, n \cdot \Delta t) &= \frac{(E_y)_{i+1/2}^n - (E_y)_{i-1/2}^n}{\Delta x} + O(\Delta x)^2 \\ \frac{\partial E_y}{\partial t}(i \cdot \Delta x, n \cdot \Delta t) &= \frac{(E_y)_i^{n+1/2} - (E_y)_i^{n-1/2}}{\Delta t} + O(\Delta t)^2\end{aligned}\tag{2.56}$$

In the Yee algorithm, the H and E components are interleaved in the space lattice at intervals of $\Delta x/2$. This approximation is called staggered grid approximation. They are also interleaved in time at intervals $\Delta t/2$. The One-dimensional formulation of the FDTD method and The orientations of H_z and E_y fields are shown as below:

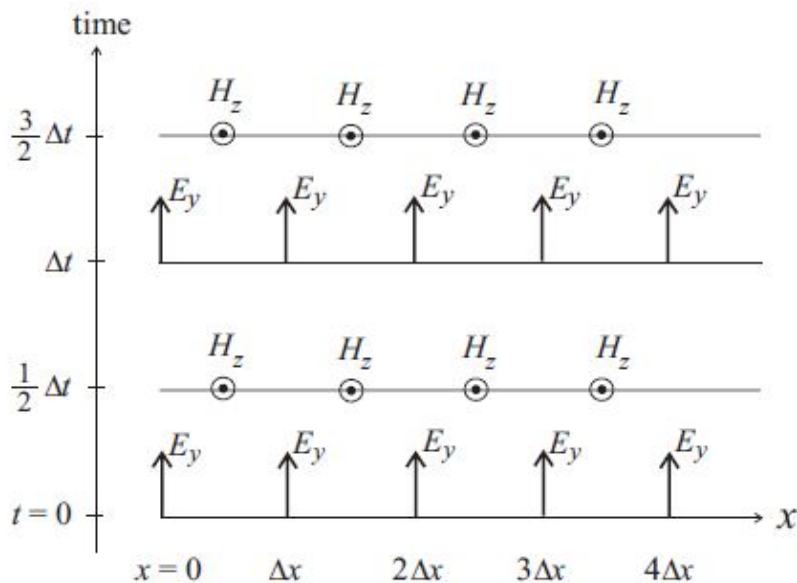


Figure 2.2: One-dimensional formulation of the FDTD method and The orientations of H_z and E_y [24]

At the time $t = 0$, values of E_y are placed at $x = i \cdot \Delta x$ with $i = 0, 1, 2, \dots, N$ for total $N + 1$ components.

At time $t = \frac{1}{2} \Delta t$, values of H_z will be placed at $x = (i - \frac{1}{2}) \cdot \Delta x$ with $i = 1, 2, 3, \dots, N$ for total N components. So in general we can write :

$$\begin{aligned} (E_y)_i^n &= E_y((i - 1) \cdot \Delta x, n \cdot \Delta t), \quad i = 1, 2, \dots, N + 1; n = 0, 1, 2, \dots \\ (H_z)_i^n &= H_z((i - \frac{1}{2}) \cdot \Delta x, (n - \frac{1}{2}) \cdot \Delta t), \quad i = 1, 2, \dots, n = 0, 1, 2, \dots \end{aligned} \quad (2.57)$$

In the most cases, we set the initial values to zero and the discretized equations are :

$$\begin{aligned} \epsilon_0 \frac{(E_y)_i^{n+1/2} - (E_y)_i^{n-1/2}}{\Delta t} &= -\frac{1}{\Delta x} ((H_z)_{i+1/2}^n - (H_z)_{i-1/2}^n) \\ \mu_0 \frac{(H_z)_{i+1/2}^{n+1} - (H_z)_{i+1/2}^n}{\Delta t} &= \frac{1}{\Delta x} ((E_y)_{i+1}^{n+1/2} - (E_y)_{i+1}^{n-1/2}) \end{aligned} \quad (2.58)$$

The space-time Independents of E_y and H_z fields at different grid points have been demonstrated below:

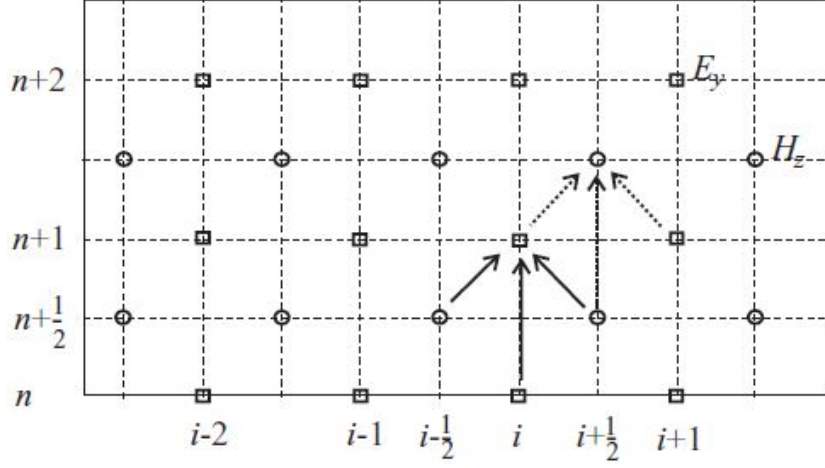


Figure 2.3: Visual illustration of numerical dependencies in the 1D FDTD method, squares represent E_y field and circles represent H_z field. [24]

One can observe that the value of a field at any point can be obtained by three previous values: two from two neighbours of opposite field from the previous half time step and one from the same field at a single previous time step.

Since the constants ϵ_0 and μ_0 in these equations differ by several orders of magnitude. Therefore, one usually introduces a new scaled variable defined as :

$$\tilde{E}_y = \sqrt{\frac{\epsilon_0}{\mu_0}} E_y \quad (2.59)$$

And we can write the scaled equations as:

$$\begin{aligned} \tilde{E}_y^{n+1/2}(i) &= \tilde{E}_y^{n-1/2}(i) - \frac{1}{\sqrt{\epsilon_0\mu_0}} \frac{\Delta t}{\Delta x} [H_z^n(i+1/2) - H_z^n(i-1/2)] \\ H_z^{n+1}(i+1/2) &= H_z^n(i+1/2) - \frac{1}{\sqrt{\epsilon_0\mu_0}} \frac{\Delta t}{\Delta x} [\tilde{E}_y^{n+1/2}(i+1) - \tilde{E}_y^{n+1/2}(i)] \end{aligned} \quad (2.60)$$

We set $\frac{\Delta x}{\Delta t} = v$ is chosen to be the maximum phase velocity of the wave expected in the medium.

2.3.2 Stability criterion

Stability criterion imposes condition on $\frac{\Delta x}{\Delta t}$ ratio known as Courant-Friedrichs-Levy (CFL) and in 1D case : $\frac{\Delta x}{\Delta t} < v$. The stability criterion summarizes the physical fact that speed of numerical propagation should not exceed the physical speed of the wave v

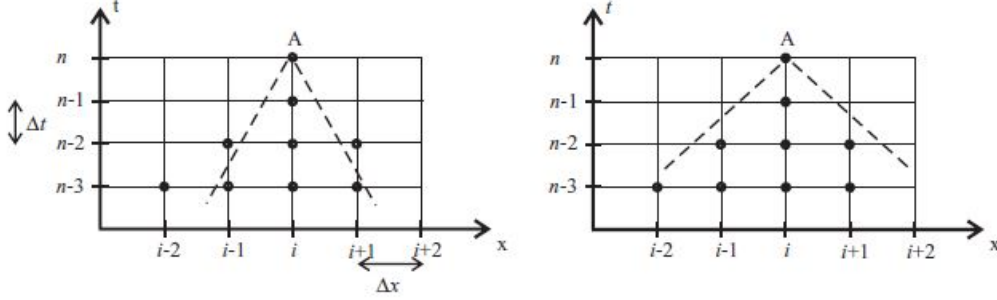


Figure 2.4: Illustration of the CFL condition. For the parameters chosen within the dashed lines, the propagation is stable (left figure) and becomes unstable (right figure.) [24]

We can summarise the stability criterion as below:

$$\begin{aligned}
 \text{1D medium} \quad & v\Delta t \leq \Delta x \\
 \text{2D medium} \quad & v\Delta t \leq \left(\frac{1}{\Delta x^2} + \frac{1}{\Delta y^2} \right)^{-1/2} \\
 \text{3D medium} \quad & v\Delta t \leq \left(\frac{1}{\Delta x^2} + \frac{1}{\Delta y^2} + \frac{1}{\Delta z^2} \right)^{-1/2}
 \end{aligned}$$

2.3.3 Material losses

In a material with losses, we have:

$$\nabla \times \mathbf{H} = \frac{\partial \mathbf{D}}{\partial t} + \sigma \mathbf{E} \quad (2.61)$$

with σ is the material conductivity, so the discretized equations become:

$$\begin{aligned}
 \frac{E_i^{n+1/2} - E_i^{n-1/2}}{\Delta t} &= -\frac{1}{\epsilon_r \sqrt{\epsilon_0 \mu_0}} \frac{H_{i+1/2}^n - H_{i-1/2}^n}{\Delta x} \\
 &\quad - \frac{\sigma}{2\epsilon_r \epsilon_0} \left(E_i^{n+1/2} + E_i^{n-1/2} \right)
 \end{aligned} \quad (2.62)$$

$$\frac{(H_2)_{i+1/2}^{n+1} - (H_2)_{i+1/2}^n}{\Delta t} = -\frac{1}{\mu_0} \frac{(E_y)_{i+1}^{n+1/2} - (E_y)_i^{n-1/2}}{\Delta x} \quad (2.63)$$

2.3.4 Boundary conditions in 1D - Absorbing boundary condition

In 1D, a generic field $\phi(x, t)$ traveling in direction $-x$ is not reflected at the left interface ($x = 0$) if:

$$\phi(0, t + \Delta t) = \phi(\Delta x, t) \quad \rightarrow t = 1 \quad (2.64)$$

Expanding $\phi(0, t + \Delta t)$ in Taylor series as:

$$\phi(0, t + \Delta t) = \phi(\Delta x, t) - \frac{\partial \phi}{\partial t} \Delta x + \frac{\partial \phi}{\partial t} \Delta z \quad (2.65)$$

knowing that $\Delta x / \Delta t = c$, which c stands for the velocity of propagating wave and substituting in the previous equations :

$$\begin{aligned} \phi(x, t) &= \phi(x, t) - \frac{\partial \phi}{\partial x} c \Delta t + \frac{\partial \phi}{\partial t} \Delta t \\ \frac{\partial \phi}{\partial x} &= \frac{1}{c} \frac{\partial \phi}{\partial t} \end{aligned} \quad (2.66)$$

Finite difference of previous equation close to the left boundary is:

$$\frac{\phi_1^{n+1/2} - \phi_0^{n+1/2}}{\Delta x} = \frac{1}{c} \frac{\phi_{1/2}^{n+1} - \phi_{1/2}^n}{\Delta t} \quad (2.67)$$

The values at half grid points and half time steps are determined as:

$$\begin{aligned} \phi_i^{n+1/2} &= \frac{1}{2} (\phi_i^{n+1} + \phi_i^n) \\ \phi_{i+1/2}^n &= \frac{1}{2} (\phi_{i+1}^n + \phi_i^n) \end{aligned} \quad (2.68)$$

Eventually we end up with the first-order Mur's absorbing boundary condition (ABC)

$$\phi_0^{n+1} = \phi_1^n + \frac{c\Delta t - \Delta x}{c\Delta t + \Delta x} (\phi_1^{n+1} + \phi_0^n) \quad (2.69)$$

A similar expression can be derived for the right side and a second order formulation of ABCs is generally used, for more details on the choosing boundary conditions, one may look [24].

2.4 Multiphysics and numerical simulations of semiconductor devices

In this part of the thesis, we focus on how the design flow and the simulation of the devices would be handled in commercial tools.

2.4.1 Structure Generation

The first step in our modelling, is generating the geometry with *SDE* or *Sentaurus Device Editor*. Via this tool, apart from the definition of the geometry, we define the doping concentrations, discretization and meshing to be used for electrical simulation and the material properties used for the device. In *sentaurus Tcad*, The *SDE* is responsible for this role and in other *Tcad* tools like *Lumerical*, each tool exploits integrated tool to define the geometry and its properties.

2.4.2 Optical simulation

After designing the geometry, The optical simulation of the device is required to obtain the absorption and generation and recombination profile to be used for the optical generation, the incident power distribution in the device in frequency domain, in this stage we are actually performing FDTD numerical simulation of the device to obtain these quantities, in this thesis, *Rsoft Fullwave* has been utilised for this aim, many research groups nowadays use *Lumerical FDTD* to optically simulate the devices and some of them uses *Matlab* so they can have enough degrees of the freedom to perform arbitrary optical simulation.

2.4.3 Electrical Simulation

Eventually at the end of the simulation flow, we use *Sdevice* tool to electrically simulate the device, first we should set the bias voltage and define the bias circuit for the device and then we can obtain the Photo current, Dark current, Frequency response and cut off frequency of the device at different input optical power to obtain the responsivity of the device. There are many other tools like *Lumerical device tool* to electrically simulate the device based on the performed FDTD simulation. these tools obtain these quantities by numerically solve the Poisson and continuity equations to obtain current densities, the simulation flow has been illustrated as below:

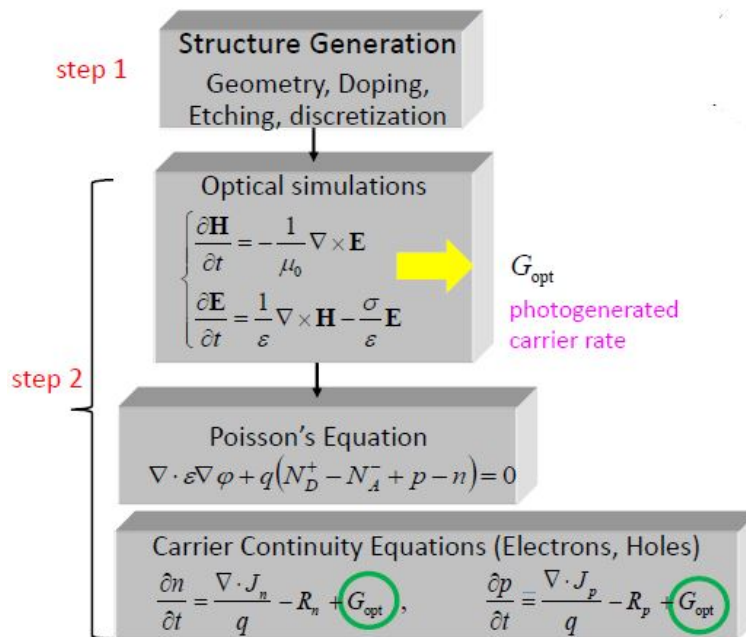


Figure 2.5: Simulation flow performed by sentaurus

Below we can see the flowchart of the steps that have to be taken to successfully simulate a semiconductor device, the key not here is that we have to perform the electromagnetic simulation in which the Maxwell equation would numerically be solved by the Tcad tool we have for the given geometry and then the results can be used for electrical simulation of the device based on Drift-Diffusion and Continuity equations. The Tcad tool we are using again use newton like method to solve mentioned equation to obtain device characteristics based on

the results of the previous step to achieve the self consistent solution of Poisson's equation.

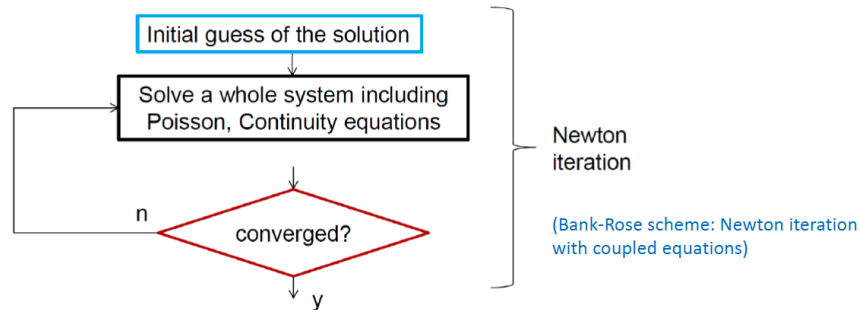


Figure 2.6: Flowchart of the numerical Newton method to solve the Poisson equation along with the continuity equations for electron and holes based on the generation rates obtained by previous step (FDTD simulation)

Moreover, it is worth to mention that we should perform the electromagnetic simulation in the absence of the electric field since affecting the generation profile by applied electric field is not desirable.

Ge-on-Si mode evolution PiN waveguide photodetectors

In this and last chapter of this thesis, we propose and investigate the two conventional structures of waveguide photodetectors (Butt-coupled and mode evolution) and their properties comparing with each other. Before starting anything, it would be of importance to devote some time the motivation behind the mode-evolution based structures and its figure of merits with respect to other structures. These kind of devices initially presented by *MIT research group in 2017* [6] and its main purpose is to serve the photodetection in the high power saturation conditions. In the mode-evolution device, the intrinsic Ge layer will be illuminated uniformly thanks to the side-coupled waveguide and this leads to decreasing saturation effects like carrier screening observable at high input powers. In this chapter, we performed electromagnetic (FDTD) and electrical simulation of the both devices to compare their performance with together. Throughout these simulation *Synopsis tools* have been utilised integrated with *Rsoft fullwave* to perform optical simulation of the devices.

3.1 Design parameters and geometry

In this part of the thesis we firstly introduce the geometry of the two devices taken from the literature [6] then we simulate and compare them together. the main difference between the aforementioned structure is the position of the waveguide which can directly affect the absorption of the light in the Ge layer which is our absorbing layer hence the overall device properties. Our model for the *Butt-coupled structure* has been shown in the below figure generated by *Sentaurus device editor*.

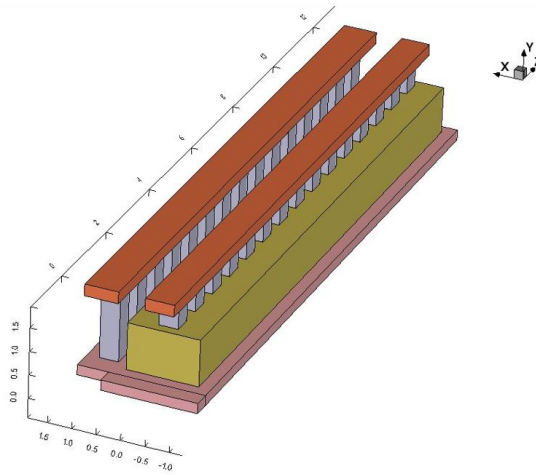


Figure 3.1: Our model for Butt-coupled structure

and our model for the *Mode evolution WPD* taken from [6] has been shown below and it has been again generated by *Sentaurus device editor or SDE*:

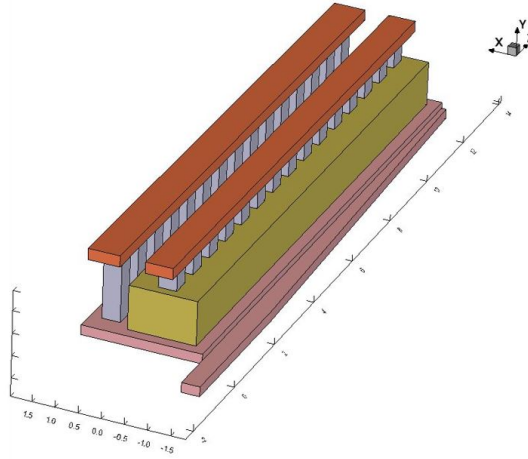


Figure 3.2: Our model for Mode evolution structure

Before moving forward , let us give some name to be used at our ease in describing the structure:

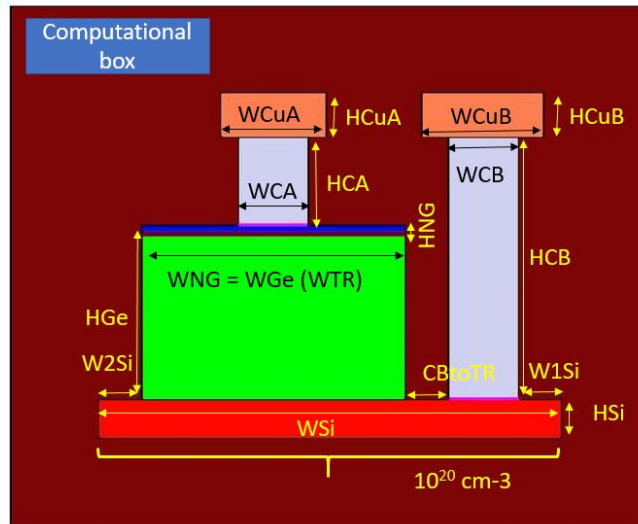


Figure 3.3: giving some names and parameters

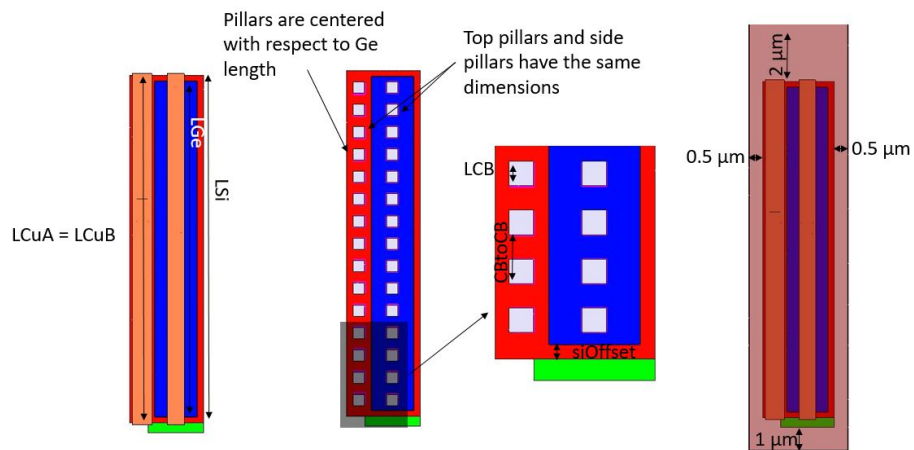


Figure 3.4: giving some names and parameters

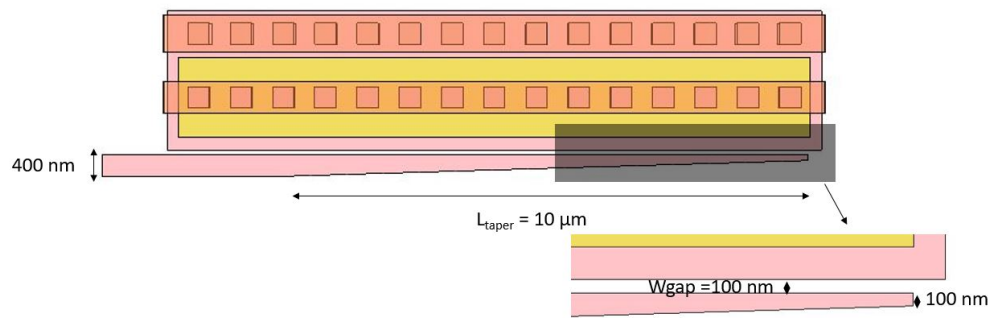


Figure 3.5: Mode evolution WPD design parameters

Geometry - X axis			
Name of quantity	Value(μm)	Name of quantity	Value(μm)
WGe	1.5	WCB	0.4
WCA	0.4	CBtoTR	0.25
WNG	1.5	WWG	2
NGinTR	0	WCuA	0.6
WSi	2.65	WCuB	0.7
W1Si	0.25	W1CuB	0.15
P2TR	Uniform doping	W2CuB	0.15
CuAtoCuB	0.5		
Geometry - Y axis			
Name of quantity	Value(μm)	Name of quantity	Value(μm)
HSi	0.22	HNG	0.05
HWG	0.22	HCuA	0.25
HTR	1	HCB	1.3
HCA	0.5	HCuB	0.25
HGe	1		
Geometry - Z axis			
Name of quantity	Value(μm)	Name of quantity	Value(μm)
LGe	12	SiOffset	0.25
NGinTR	0	OffsetCB	0.5
CAinTR	0.25	CBtoCB	0.8
LCB	0.4	Number of W pillars	15
LCuA	12.5	LCuB	12.5

3.2 Simulation and analysis approach

The geometry is generated with SDE tool, considering a worst case approach, i.e. the Ge on the Si substrate is considered bulk material, i.e. no strain is applied to the Ge, so there is no improvements in the absorption profile of the Ge at higher .

The geometry generated with SDE is used as input of the optical solver, RSoft FullWave, which simulates light propagation in the devices. A quite large computational box is needed, and a very dense mesh is required in order to get an accurate result. A uniform mesh in all directions is chosen, with very low Δr (i.e. distance between one point and the following one). Below 40nm the solution of the optical problem obtained is invariant with respect to the chosen mesh size. Therefore, a mesh size of 25nm is chosen. From the simulation perspective, this value is convenient since it is a multiple of all the dimensions of each component of the two configuration, eliminating the uncertainty at boundaries. As boundary condition for the optical problem, perfect matched layer (PML) boundary conditions are chosen. This kind of boundaries can be configured to absorb (ideally) all the light impinging on them, so that no reflected light from the boundary should be present. Since metals contribute only with a power loss to the optical problem, they have been described as perfect electrical conductors (PEC). Silicon is practically transparent at the two studied wavelength, in fact only the Ge detector is highly influenced by the optical field. Indeed, the Ge detector absorbs light and this triggers the generation process of electron-hole pairs.

The mode light source used in the simulations is computed by the FDTD tool as a preliminary step, and then this is propagated in the waveguide/device. This procedure helps reducing noise and interference, since, if the mode is confined in the waveguide, practically no light may escape the waveguide and it is directly guided to the detector.

Once the optical power in the Ge detector is evaluated, it is used as a generation-recombination rate in the drift diffusion solver. RSoft provides an utility that converts automatically the results taking care of the different material parameters. The bias point is computed, as well as the dark current, with sDevice tool. A reverse bias voltage of 3V is chosen and all other computation are based on this bias point. The responsivity is computed as the derivative of the power-

current (PI) curve, but since it is linear, it has been simplified with the difference of two points corresponding to minimal and maximal input power respectively. Finally, the frequency response is found with a resistive load equal to 50Ω that is connected at one of the two pins of the photodiode, so that capacitive effects are noticeable.

In addition, it is important to know that in this approach we do not try to achieve a truly self-consistent solution to the Poisson equation since achieving such a goal is computationally expensive and time consuming for the simulation specifications we have in this project as well as the device geometry

3.3 Simulation results- Butt-coupled waveguide photodetector

The numerical and multi physic simulation of the MIT butt coupled WPD has been carried out with synopsis tools, based on what we demonstrated before , first we define the geometry followed by optical simulation of the device for the light with input optical power of $200 \mu W$, the optical generation rate for the butt coupled structure for the 3 main wavelengths 1310 nm , 1550 nm and 1520 nm has been shown in logarithmic and linear scale below:

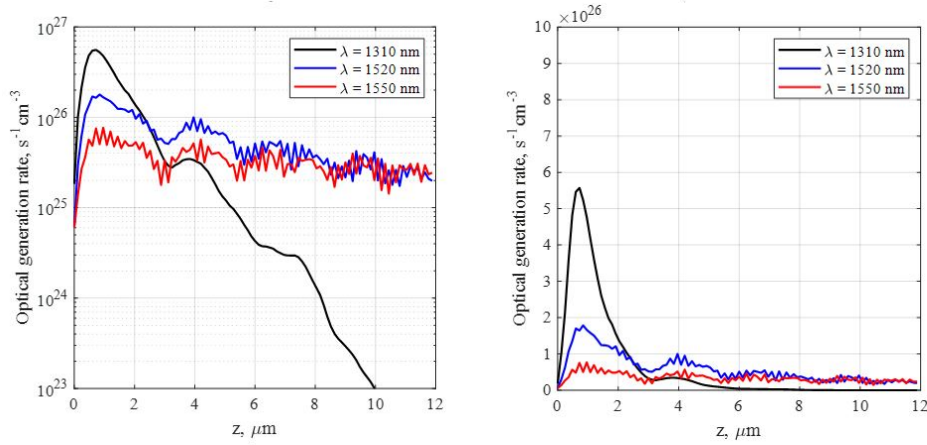


Figure 3.6: Optical generation rate in linear(right) and logarithmic(left) scale for butt coupled structure

We can see that due to the geometry of the device, the generation rate experience a peak in the interface of the waveguide and substrate and then the will decrease gradually. The obvious thing is we should expect a lower responsivity in the case of 1310 nm since the generation rate will undergo a significant increase along the Z axis.

Turning to responsivity of the device , the PI curve of the device has been shown below, by definition the responsivity is the slope of the PI curve as it was illustrated before the Ch.1.

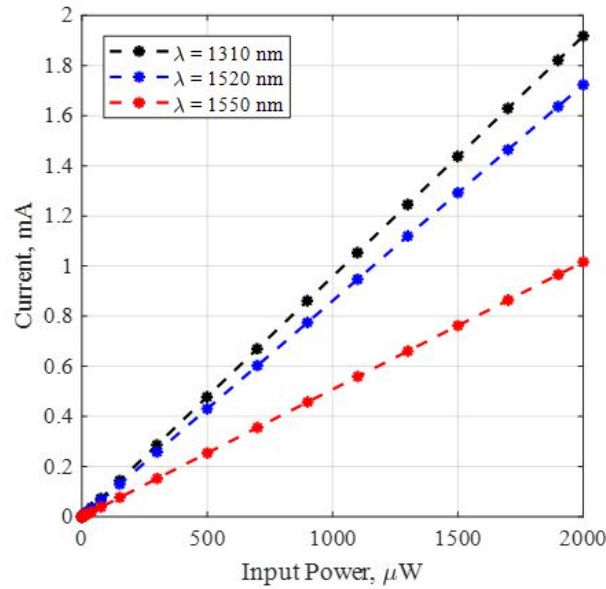


Figure 3.7: PI curve of the butt coupled WPD

We can see that the highest value of the responsivity has been obtained for the 1310 nm and it would decrease with increase of the incident wavelength.

Lastly, turning to the device’s frequency response, it was carried out by Sdevice and it is reported as below:

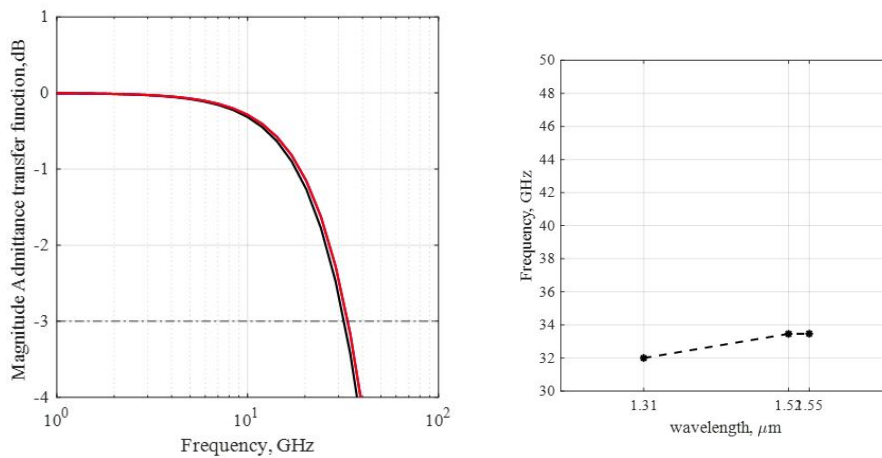


Figure 3.8: Frequency response of the butt coupled WPD

3.4 Mode Evolution waveguide photodetectors simulation results

In a mode evolution photodetector the waveguide structure is different with respect to butt coupled WPD and it is parallel to the Ge detector. Since a gap of $0.1 \mu\text{m}$ is present between the substrate and the waveguide, there is no direct coupling, and the light is coupled through the evanescent field to the detector. This allows to achieve good performance and a good distribution of the input optical field in the Ge detector. We repeated the simulation we performed for the BC structure and obtained the below results. The optical generation rates for linear and logarithmic scale has been reported:

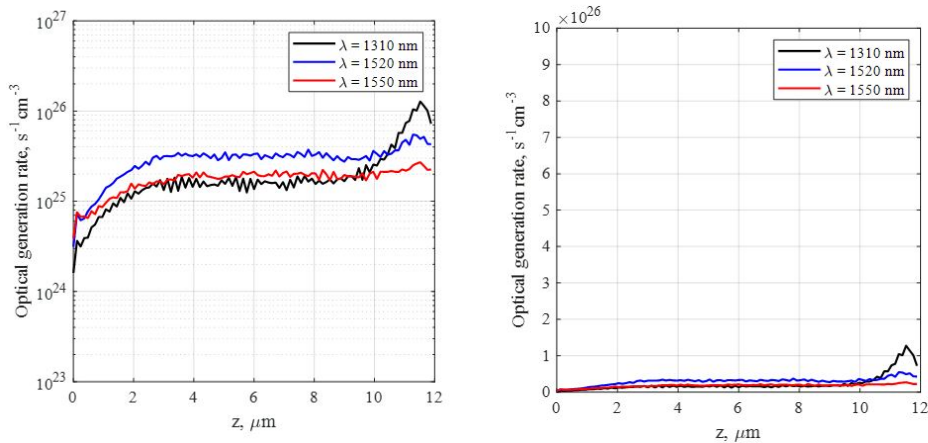


Figure 3.9: Optical generation rate in linear(right) and logarithmic(left) scale for Mode evolution structure

We can see that The optical generation rate is gradually increasing at the beginning of the detector. This effect is related to the coupling of the optical field: the taper which its front end is a 100 nm rectangle present at the end of the waveguide is orienting the light inside the detector along the z axis, so at the beginning very little portion of light is present inside the detector. Now we can report the simulated responsivity of the device and compare it with the values indicated in [6].

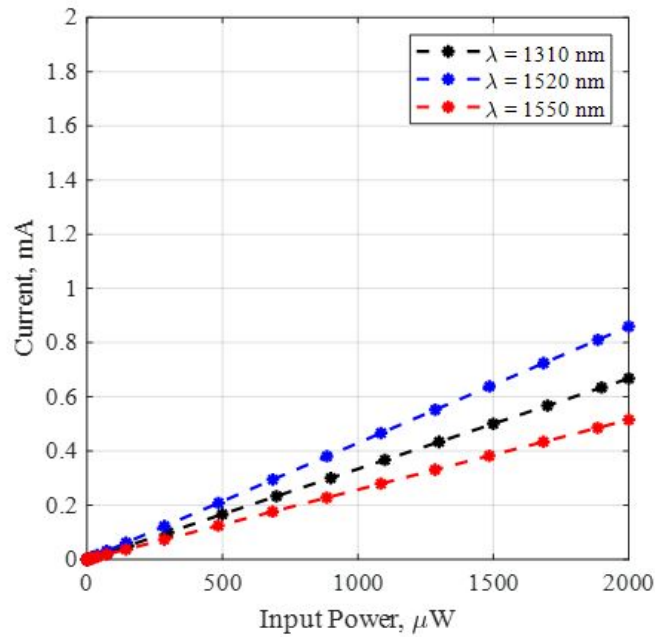


Figure 3.10: PI curve of the Mode evolution WPD

The first thing to be noticed is that the responsivity is lower than the case butt-coupled and the second thing is that the simulated results are lower than what have been reported in [6], as we proceed , in the conclusion section, we will explain the effort we made to make the results closer to literature.

Eventually , turning to the frequency response, the results have been demonstrated as below:

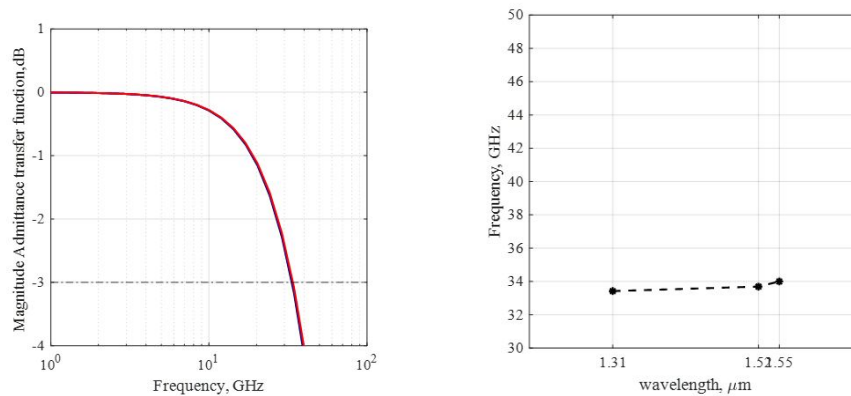


Figure 3.11: Frequency response and cut off frequency of Mode evolution structure

As it is clear, the frequency response is almost the same for the 3 wavelengths

we simulated the device.

3.5 Conclusion

We have seen two kind of WPD so far with different geometries and properties, in this last part of this thesis we compare them together and propose some simulation techniques in order to enhance the device. First of all, we superimposed all the plots related to different properties of the WPD to see their comparisons.

The first quantity we want to investigate is optical generation rate, we can see all optical generations:

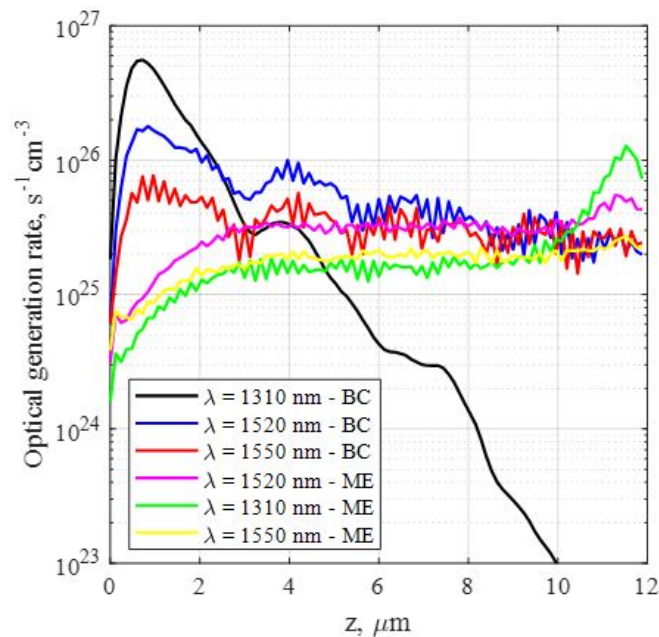


Figure 3.12: Optical generation rates in Log scale

We can see that at the beginning of the device, the optical generation rate is higher in BC case and this is due to the geometry of the waveguide in the two cases.

Turning to frequency response and cut off frequency we can see that mode evolution case shows higher cut off frequency in comparison with the BC case and the trend is decreasing in both cases and the values are almost consistent with the values reported in [6].

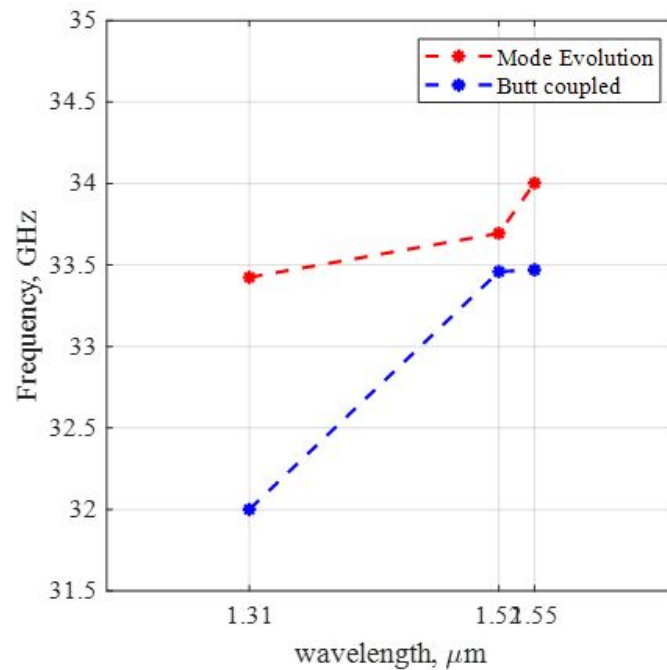


Figure 3.13: Cut of frequency for all cases

The responsivity has been reported for the two case in the figure below:

We can see that the responsivity is higher in the BC case for the input optical power of $200 \mu\text{W}$ and it decreases with increase of the wavelength for both cases, in the case of the mode evolution case, the responsivity is lower than the values reported in the [6], this could have a few possible explanation such as :

- Back reflection in the boundaries in the simulation of the device.
- the specifications of the Ge which is used in the paper is different that the one we used in our simulations

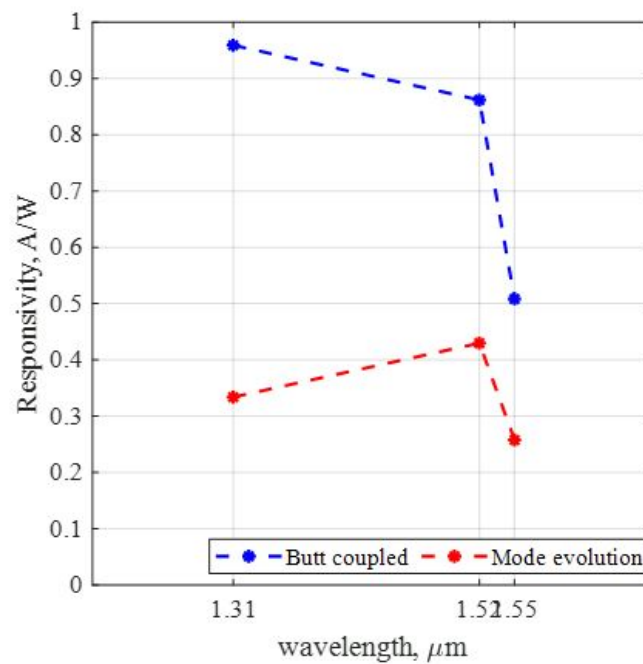
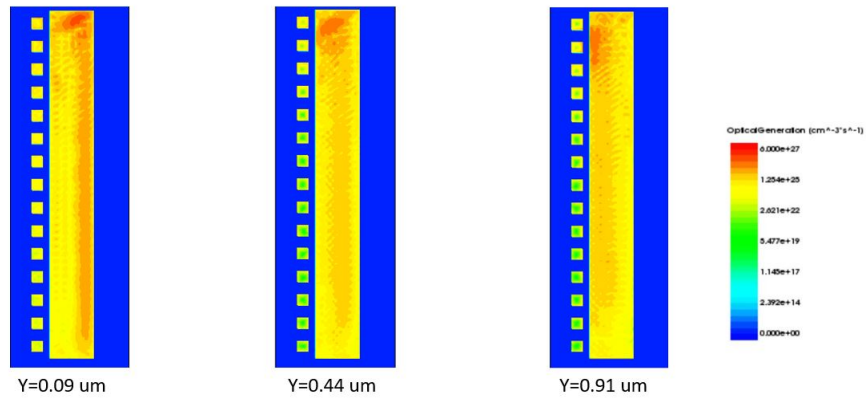


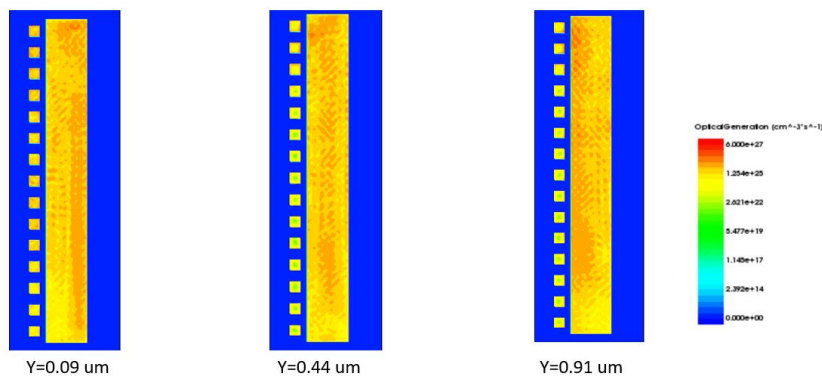
Figure 3.14: Responsivity for the all cases

To investigate the first assumption, knowing that we use PML boundary conditions for all of our simulations, multiple time monitors were used to investigate the effect of the back reflections in the device. for this aim, we add another monitor in Rsoft full-wave Tcad environment and we set the parameter phi equal to 180 degree to monitor the absorption profile for the two directions.

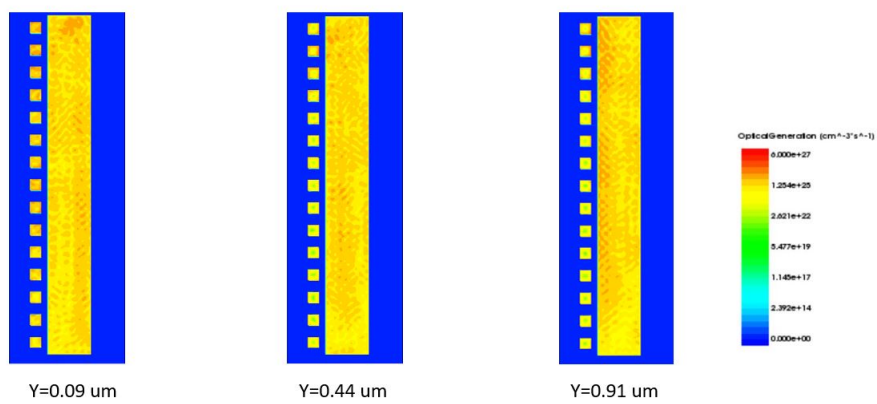
the colour map for different cut-planes have been reported as below,

Mode-evolution:For the case $\phi = 0$:

(a) 1310 nm



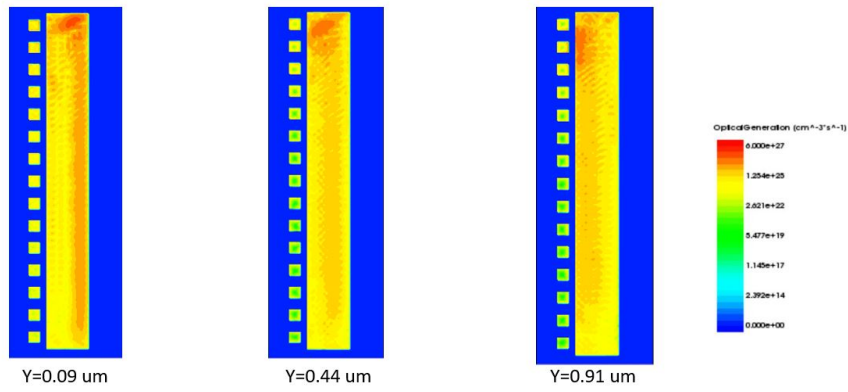
(a) 1520 nm



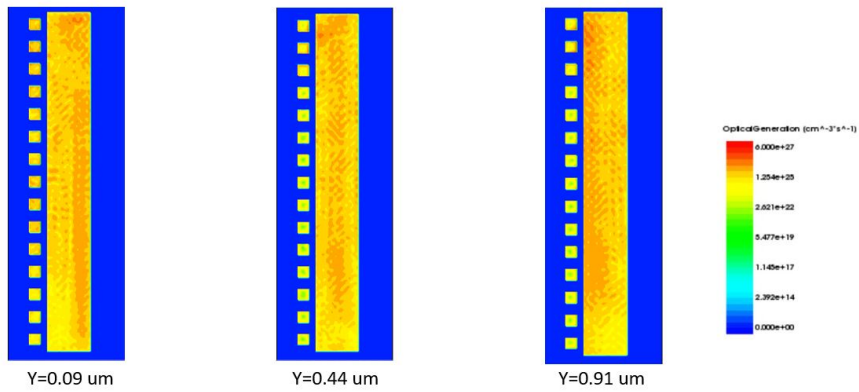
(a) 1550 nm

3. Ge-on-Si mode evolution PiN waveguide photodetectors

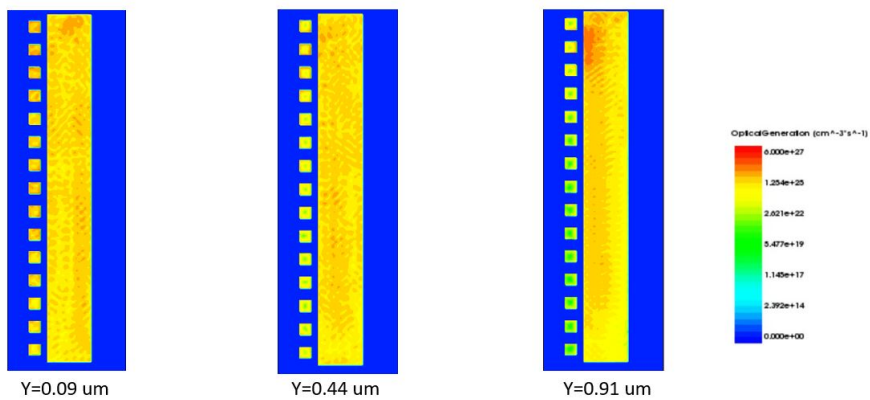
For the case $\Phi = 180^\circ$:



(a) 1310 nm

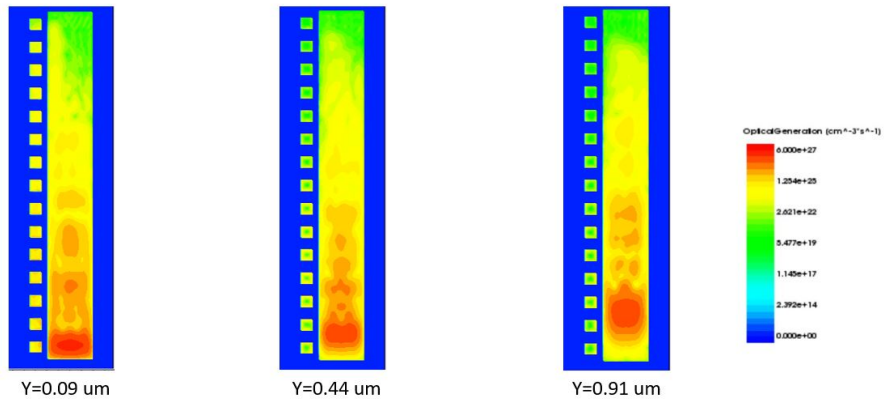


(a) 1520 nm

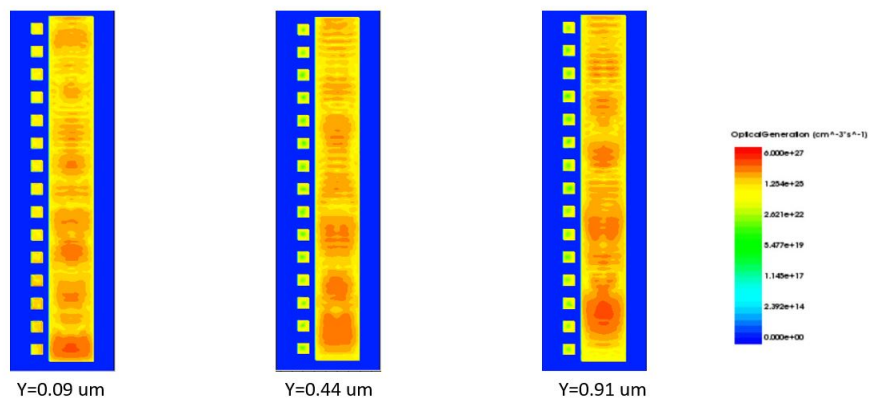


(a) 1550 nm

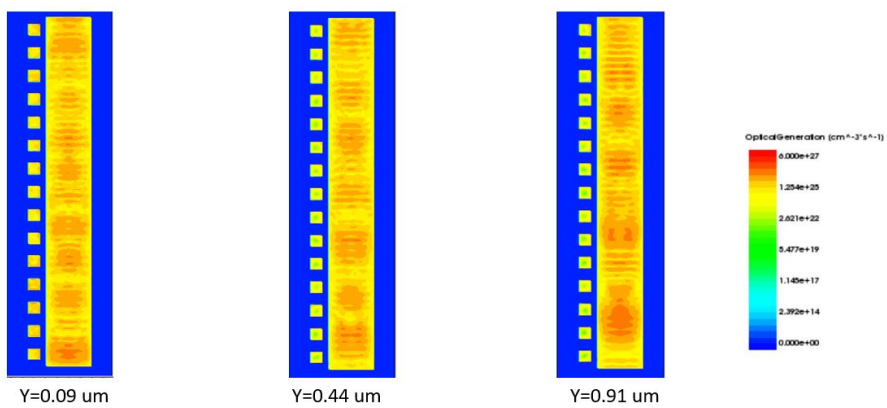
Butt-coupled:
for the case $\phi = 0$:



(a) 1310 nm



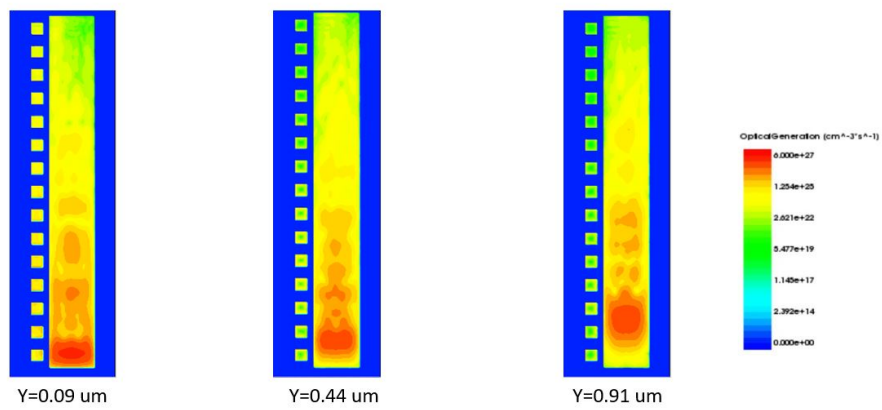
(a) 1520 nm



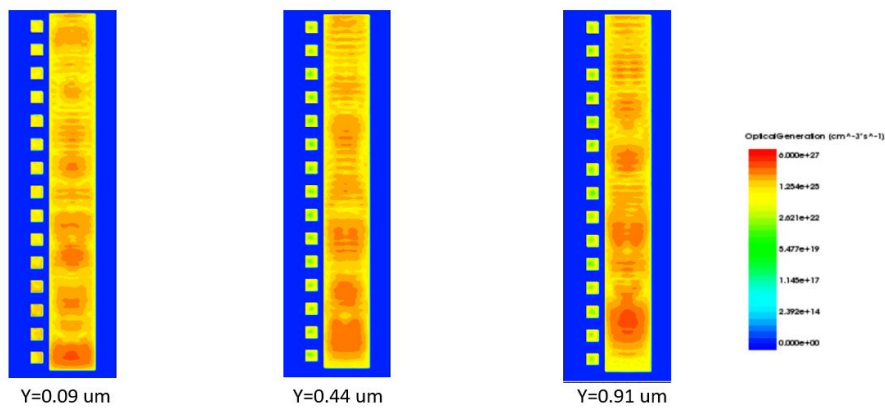
(a) 1550 nm

3. Ge-on-Si mode evolution PiN waveguide photodetectors

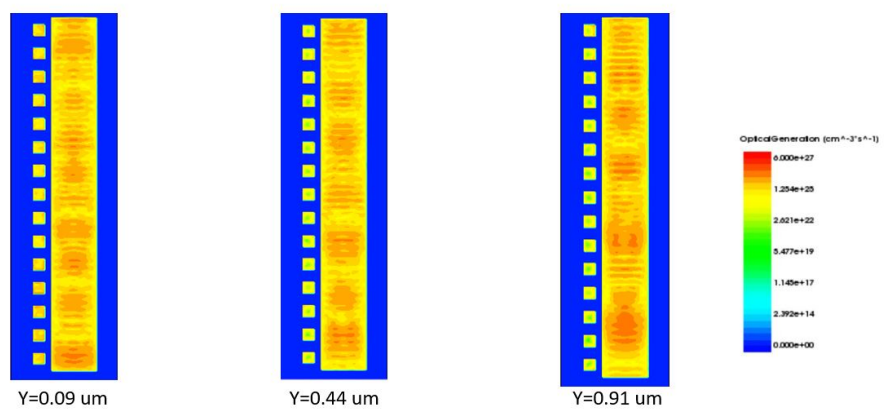
and for the case $\phi = 180^\circ$:



(a) 1310 nm



(a) 1520 nm



(a) 1550 nm

So according to the colour maps we can see that the PML boundary conditions works well in our simulation and the reason of deviation in the results for the case mode evolution, could be the conditions which were implied on the Ge such as strain or other parameters which could affect the Ge absorption profile. In addition, it was observed that as we change the front end of the coupling waveguide from triangular to a rectangle with of 100 nm, the simulations underwent coupling and converging issues.

Bibliography

- [1] *Wikipedia, Maxwell's equations.*
- [2] Daniel Benedikovic, Léopold Viro, Guy Aubin, Farah Amar, Bertrand Szelag, Bayram Karakus, Jean-Michel Hartmann, Carlos Alonso-Ramos, Xavier Le Roux, Paul Crozat, et al. 25 gbps low-voltage hetero-structured silicon-germanium waveguide pin photodetectors for monolithic on-chip nanophotonic architectures. *Photonics Research*, 7(4):437–444, 2019.
- [3] Daniel Benedikovic, Leopold Viro, Guy Aubin, Farah Amar, Bertrand Szelag, Bayram Karakus, Jean-Michel Hartmann, Carlos Alonso-Ramos, Xavier Le Roux, Paul Crozat, et al. High-performance waveguide photodetectors based on lateral si/ge/si heterojunction. In *Integrated Optics: Devices, Materials, and Technologies XXIII*, volume 10921, page 109210O. International Society for Optics and Photonics, 2019.
- [4] Daniel Benedikovic, Léopold Viro, Guy Aubin, Jean-Michel Hartmann, Farah Amar, Xavier Le Roux, Carlos Alonso-Ramos, Eric Cassan, Delphine Marris-Morini, Paul Crozat, et al. 40 gbps heterostructure germanium avalanche photo receiver on a silicon chip. *Optica*, 7(7):775–783, 2020.
- [5] Daniel Benedikovic, Léopold Viro, Guy Aubin, Jean-Michel Hartmann, Farah Amar, Bertrand Szelag, Xavier Le Roux, Carlos Alonso-Ramos, Paul Crozat, Eric Cassan, et al. 28 gbps silicon-germanium hetero-structure avalanche photodetectors. In *Integrated Optics: Devices, Materials, and Technologies XXIV*, volume 11283, page 112830Y. International Society for Optics and Photonics, 2020.

-
- [6] Matthew J Byrd, Erman Timurdogan, Zhan Su, Christopher V Poulton, Nicholas M Fahrenkopf, Gerald Leake, Douglas D Coolbaugh, and Michael R Watts. Mode-evolution-based coupler for high saturation power ge-on-si photodetectors. *Optics letters*, 42(4):851–854, 2017.
- [7] Hong Tao Chen, Peter Verheyen, Peter De Heyn, Guy Lepage, Jeroen De Coster, Philippe Absil, Gunther Roelkens, and Joris Van Campenhout. High-responsivity low-voltage 28-gb/s ge pin photodetector with silicon contacts. *Journal of Lightwave Technology*, 33(4):820–824, 2014.
- [8] Hongtao Chen, P Verheyen, P De Heyn, G Lepage, J De Coster, S Balakrishnan, P Absil, W Yao, L Shen, Günther Roelkens, et al. - 1 v bias 67 ghz bandwidth si-contacted germanium waveguide pin photodetector for optical links at 56 gbps and beyond. *Optics Express*, 24(5):4622–4631, 2016.
- [9] Seongjae Cho, Stanley S Cheung, Yung Hun Jung, Sae-Kyoung Kang, Dal Ho Lee, and Byung-Gook Park. Ge-on-si photodetector with enhanced optical responsivity by advanced metallization geometry. *JOURNAL OF SEMICONDUCTOR TECHNOLOGY AND SCIENCE*, 20(4):367, 2020.
- [10] Jishi Cui, Tiantian Li, Fenghe Yang, Wenjing Cui, and Hongmin Chen. The dual-injection ge-on-si photodetectors with high saturation power by optimizing light field distribution. *Optics Communications*, page 126467, 2020.
- [11] Jishi Cui and Zhiping Zhou. High-performance ge-on-si photodetector with optimized dbr location. *Optics Letters*, 42(24):5141–5144, 2017.
- [12] Qian Ding, Saurabh Sant, and Andreas Schenk. Design strategy for monolithically integrated photodetector and improvement using plasmonics. In *2019 International Conference on Numerical Simulation of Optoelectronic Devices (NUSOD)*, pages 155–156. IEEE, 2019.
- [13] Qian Ding, Saurabh Sant, and Andreas Schenk. Scaling effects on the plasmonic enhancement of butt-coupled waveguide photodetectors. In *2020 International Conference on Numerical Simulation of Optoelectronic Devices (NUSOD)*, pages 29–30. IEEE, 2020.

- [14] Ning Duan, Tsung-Yang Liow, Andy Eu-Jin Lim, Liang Ding, and Guo Qiang Lo. High speed waveguide-integrated ge/si avalanche photodetector. In *Optical Fiber Communication Conference*, pages OM3K–3. Optical Society of America, 2013.
- [15] Monireh Moayedipour Fard, Glenn Cowan, and Odile Liboiron-Ladouceur. Responsivity optimization of a high-speed germanium-on-silicon photodetector. *Optics Express*, 24(24):27738–27752, 2016.
- [16] Giovanni Ghione. *High-speed semiconductor devices and circuits*. Cambridge University Press, 2009.
- [17] Ryan Going, Tae Joon Seok, Jodi Loo, Kyle Hsu, and Ming C Wu. Germanium wrap-around photodetectors on silicon photonics. *Optics Express*, 23(9):11975–11984, 2015.
- [18] Chong Li, Shihong Qin, Ben Li, Kai Bao, and Jiale Su. Enhancement of responsivity and speed in waveguide ge/si avalanche photodiode with separate vertical ge absorption, lateral si charge and multiplication configuration. *Optical and Quantum Electronics*, 51(7):219, 2019.
- [19] Xiu-Li Li, Zhi Liu, Lin-Zhi Peng, Xiang-Quan Liu, Nan Wang, Yue Zhao, Jun Zheng, Yu-Hua Zuo, Chun-Lai Xue, and Bu-Wen Cheng. High-performance germanium waveguide photodetectors on silicon. *Chinese Physics Letters*, 37(3):038503, 2020.
- [20] Yuji Miyasaka, Tatsuro Hiraki, Kota Okazaki, Kotaro Takeda, Tai Tsuchizawa, Koji Yamada, Kazumi Wada, and Yasuhiko Ishikawa. Ge/graded-sige multiplication layers for low-voltage and low-noise ge avalanche photodiodes on si. *Japanese Journal of Applied Physics*, 55(4S):04EH10, 2016.
- [21] Synopsys. *Rsoft Fullwave manual v2017.09*.
- [22] S.M. Sze and Kwok K. Ng. *Physics of Semiconductor Devices*. John Wiley & Sons, Inc., apr 2006.

- [23] Tapani Vehmas, Markku Kapulainen, Päivi Heimala, Giovanni Delrosso, Fei Sun, Feng Gao, and Timo Aalto. Monolithic integration of up to 40 ghz ge photodetectors in 3um soi. In *Silicon Photonics XV*, volume 11285, page 112850V. International Society for Optics and Photonics, 2020.
- [24] Marek S Wartak. *Computational photonics: an introduction with MATLAB*. Cambridge University Press, 2013.
- [25] Wenzhou Wu, Buwen Cheng, Jun Zheng, Zhi Liu, Chuanbo Li, Yuhua Zuo, and Chunlai Xue. High gain-bandwidth product ge/si tunneling avalanche photodiode with high-frequency tunneling effect. *Journal of Semiconductors*, 38(11):114003, 2017.
- [26] Kane Yee. Numerical solution of initial boundary value problems involving maxwell's equations in isotropic media. *IEEE Transactions on antennas and propagation*, 14(3):302–307, 1966.
- [27] H Zegmout, B Szelag, S Bernabé, L Viot, P Grosse, Q Wilmart, and S Brisson. High speed integrated waveguide lateral si/ge/si photodiodes with optimized transit time. In *Silicon Photonics XV*, volume 11285, page 1128515. International Society for Optics and Photonics, 2020.
- [28] Haifeng Zhou and Yiling Sun. Size reduction of ge-on-si photodetectors via a photonic bandgap. *Applied optics*, 57(12):2962–2966, 2018.